SANDIA REPORT

SAND2005-6524
Unlimited Release
Printed November 2005

Assembly and Actuation of Nanomaterials Using Active Biomolecules

George D. Bachand, Bruce C. Bunker, Susan B. Rivera, Andrew K. Boal, Marlene Bachand, Amanda M. Trent, Erik D. Spoerke, Jun Liu, Darryl Y. Sasaki, Steven J. Koch, Jennifer M. Gaudioso, Gayle E. Thayer, Alex D. Corwin, Maarten P. de Boer

Prepared by
Sandia National Laboratories
Albuquerque, New Mexico 87185 and Livermore, California 94550

Sandia is a multiprogram laboratory operated by Sandia Corporation,
a Lockheed Martin Company, for the United States Department of Energy's
National Nuclear Security Administration under Contract DE-AC04-94AL85000.

Issued by Sandia National Laboratories, operated for the United States Department of Energy by Sandia Corporation.

Available to DOE and DOE contractors from
U.S. Department of Energy
Office of Scientific and Technical Information
P.O. Box 62
Oak Ridge, TN 37831

Telephone: (865)576-8401
Facsimile: (865)576-5728
E-Mail: reports@adonis.osti.gov
Online ordering: http://www.osti.gov/bridge

Available to the public from
U.S. Department of Commerce
National Technical Information Service
5285 Port Royal Rd
Springfield, VA 22161

Telephone: (800)553-6847
Facsimile: (703)605-6900
E-Mail: orders@ntis.fedworld.gov
Online order: http://www.ntis.gov/help/ordermethods.asp?loc=7-4-0#online

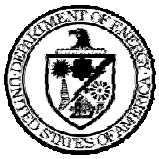

SAND2005-6524
Unlimited Release
Printed November 2005

Assembly and Actuation of Nanomaterials Using Active Biomolecules

George D. Bachand, Bruce C. Bunker, Andrew K. Boal, Marlene Bachand, Amanda M. Trent, Darryl Y. Sasaki, Steven J. Koch, Gayle E. Thayer
Biomolecular Interfaces & Systems Department

Susan B. Rivera, Jennifer M. Gaudioso
Chem-Bio Nonproliferation Department

Jun Liu, Erik Spoerke
Electronic & Nanostructured Materials Department

Alex Corwin
MEMS and Novel Silicon Technologies Department

Maarten P. de Boer
MEMS Devices & Reliability Physics Department

Sandia National Laboratories
P.O. Box 5800, MS1413
Albuquerque, NM 87185-1413

Abstract

The formation and functions of living materials and organisms are fundamentally different from those of synthetic materials and devices. Synthetic materials tend to have static structures, and are not capable of adapting to the functional needs of changing environments. In contrast, living systems utilize energy to create, heal, reconfigure, and dismantle materials in a dynamic, non-equilibrium fashion. The overall goal of the project was to organize and reconfigure functional assemblies of nanoparticles using strategies that mimic those found in living systems. Active assembly of nanostructures was studied using active biomolecules to drive the organization and assembly of nanocomposite materials. In this system, kinesin motor proteins and microtubules were used to direct the transport and interactions of nanoparticles at synthetic interfaces. In

addition, the kinesin/microtubule transport system was used to actively assemble nanocomposite materials capable of storing significant elastic energy. Novel biophysical measurement tools were also developed for measuring the collective force generated by kinesin motor proteins, which will provide insight on the mechanical constraints of active assembly processes. Responsive reconfiguration of nanostructures was studied in terms of using active biomolecules to mediate the optical properties of quantum dot (QD) arrays through modulation of inter-particle spacing and associated energy transfer interaction. Design rules for kinesin-based transport of a wide range of nanoscale cargo (e.g., nanocrystal quantum dots, micron-sized polymer spheres) were developed. Three-dimensional microtubule organizing centers were assembled in which the polar orientation of the microtubules was controlled by a multi-staged assembly process. Overall, a number of enabling technologies were developed over the course of this project, and will drive the exploitation of energy-driven processes to regulate the assembly, disassembly, and dynamic reorganization of nanomaterials.

Acknowledgments

This work was supported by Sandia's Laboratory Directed Research and Development (LDRD) Project 52531. Sandia is a multiprogram laboratory operated by Sandia Corporation, a Lockheed Martin Company, for the United States Department of Energy under Contract DE-AC04-94AL85000.

Table of Contents

1.0 General Introduction

The synthesis/construction of nanoscale materials and devices may be achieved using two generalized approaches: (1) "top-down," and (2) "bottom-up." In the first approach, structural, nanoscale features are defined in bulk materials using lithographic or imprinting techniques analogous to those employed in silicon micromachining. Although quite useful, many of these techniques are inherently slow and often expensive. "Bottom-up" approaches utilize self-assembly of individual molecules to form complex, nanostructured materials. The resulting materials, however, are commonly heterogeneous in structure due to the underlying equilibrium constraints.

The strategies used to assemble and organize nanomaterials in living organisms are fundamentally different from the self-assembly strategies used in synthetic materials and systems. A key difference in the two strategies is the ability of living organisms to utilize energy to assemble materials capable of rearranging, repairing, and adapting based on environmental and physiological stimuli. Such direct energy utilization enables the assembly/disassembly of much more complex, non-equilibrium structures that overcome enthalpic, entropic, and diffusional barriers that inhibit standard self-assembly processes. The goal of this project was to explore the active assembly and actuation of nanomaterials using active biomolecules. Because these processes involved a wide array of highly complex, regulated, and interconnected systems, our work focused specifically on the kinesin/microtubule system, as a model system for understanding and exploiting energy-driven nanoscale transport systems.

Active transport systems in living systems play key roles in a wide array of physiological process including energy conversion, cellular repair, and muscle actuation. In particular, the kinesin/microtubule system is primarily responsible for the directed trafficking of macromolecule materials within a cell, removing the constraints inherent to diffusion within a gel. In many cases, such directed transport of materials leads to macroscopic, phenotypic responses at the cellular or organismal level. For example, the ability of fish and other organisms to change color (a macroscopic response) involves the energy-drive assembly and organization of pigment granules by kinesin and microtubule (a nanoscale process). Kinesin-based transport also has been implicated in the active transport of amorphous silica in diatomaceous algae, which in turn is used to assemble the complex, protective "skeletons" of these organisms. In the long-term, understanding how Nature utilizes such energy-driven assembly processes for "bottom-up" materials assembly will help enable the design and engineering of analogous strategies for developing novel nanomaterials.

This report summarizes major accomplishments over the course of this three-year LDRD project. The report is divided into five independent sections that present key technology development and fundamental science, including: (1) assembling and transporting nanocrystal quantum dot nanocomposites, (2) determining the physical factors affecting transport of synthetic nanoparticle cargo, (3) characterizing the interactions between cargo-carrying biomolecular shuttles, (4) assembling artificial three-dimensional microtubule organizing centers, and (5) engineering micromachined force sensors for biophysics measurements.

2.0 Assembly and transport of nanocrystal CdSe quantum dot nanocomposites using microtubules and kinesin motor proteins

George D. Bachand, Susan B. Rivera, Andrew K. Boal, Jennifer Gaudioso, Jun Liu, and Bruce C. Bunker

2.1 Abstract

Nature has evolved dynamic, non-equilibrium mechanisms for assembling hierarchical complexes of nanomaterials. A critical element to many of these assembly mechanisms involves the active and directed transport of materials by biomolecular motor proteins such as kinesin. In the present work, nanocrystal quantum dots (nQDs) were assembled and organized using microtubule (MT) filaments as nanoscale scaffolds. nQD density and localization were systematically evaluated by varying the concentration and distribution of functional groups within the MT structure. Confining nQD attachment to a central region within the MT enabled unaffected interaction with kinesin necessary to support active transport of nQD-MT composites. This active transport system will be further refined to control the optical properties of a surface by regulating the collective organization of nQD-MT composites.

2.2 Introduction

The formation and intrinsic properties of materials from living systems are inherently different than those of synthetic materials. While synthetic materials may be self-assembled using equilibrium-regulated processes, Nature has developed a wide array of non-equilibrium based strategies for directing the assembly and adaptive organization of materials at the nano- and molecular scale. Exploiting such strategies for use in composite nanomaterials may permit the incorporation of dynamic and adaptive properties based on biomimetic assembly processes[1,2]. A key aspect in these strategies is the ability to direct the assembly, transport, and organization of materials at specific locations.

The biomolecular motor kinesin has been well studied with respect to its role in actively transporting intracellular materials (e.g., vesicles, chromosomes) along cytoskeletal networks composed of microtubule (MT) filaments[3,4]. Conventional kinesin moves along MT filaments in 8-nm steps by alternating between two conformational states in an asymmetric hand-over-hand mechanism[5,6]. Further, the processive nature of kinesin movement along MTs enables long-distance transport of molecular cargo, a critical function, for example, in neuronal cells. Kinesin and MT filaments also interact to self-assemble complex, three-dimensional structures such as the mitotic spindles formed during mitosis[7,8]. The force generated by kinesin and MTs are subsequently used to segregate chromosomes during the anaphase stage of mitosis. The dynamic nature and forces produced by kinesin and MTs also play an important role in reorganization of nanoscale materials in living systems, such as the melanophores that induce color change in fish[9].

Based on the broad role that kinesin and MTs play in living organisms, modified versions on this system have been investigated as a means of transporting synthetic

nanoscale cargo in integrated systems[10-12]. Such directed transport systems may be ideally suited for developing nanostructured materials in which the morphology and configuration of base materials can be regulated through non-equilibrium assembly processes. Although MTs can be readily functionalized with inorganic materials[13-16], the kinesin-based active transport mechanism is disrupted due to interference caused by the inorganic coating. In order to preserve unimpeded interaction with surface-tethered kinesin that provide motion, it is essential that the assembly and organization of nanoscale materials on MTs be systematically controlled and evaluated. To this end, two key challenges surrounding the assembly and transport of composite MT-nanoparticle structures must be addressed: (1) insuring that a nanoparticle interacts with only a single MT (i.e., preventing agglomeration), and (2) insuring that nanoparticle cargo does not affect binding and transport by kinesin. To investigate these issues, we assembled a variety of nanocomposite structures using MT filaments as nanoscale scaffolds, and evaluated the ability of kinesin to transport these structures. Here we report the assembly and organization of CdSe nanocrystal quantum dots (nQDs) using MT filaments. Unabated, kinesin-based transport of linear chains of nQDs on MTs was subsequently demonstrated by modifying the MT structure, and localizing nQD binding. Extension of this technology may permit the incorporation of active and dynamic nQD structures in a host of biocompatible devices and materials.

2.3 Assembly of nanocomposites using MT scaffolds

Two strategies were used to assemble composite structures using MT filaments to organize CdSe nQDs. Biotin-streptavidin linkage was used in both strategies to couple nQDs to MTs based upon the high-binding affinity and commercial availability of the functionalized CdSe nQDs. In the first strategy, the relationship between biotin concentration in a MT and the formation of nQDs structures was systematically evaluated. To regulate the density of the nQD cargo, the concentration of biotinylated tubulin was varied between 0 and 100% by adjusting the ratio of biotinylated to unlabeled tubulin. Random incorporation of biotinylated tubulin into MTs during polymerization resulted in MTs with final biotin concentrations of 0, 6.25%, 12.5%, 25%, 50%, and 100%. In all cases, 20 μg of unlabeled/biotinylated tubulin (Cytoskeleton Inc., Denver, CO) was suspended in 4 μl of BRB80P (80 mM PIPES pH 6.9, 1 mM $MgCl_2$, 1mM EGTA, 10% glycerol, 1 mM GTP), and then polymerized at 37°C for 20 min. Polymerized MTs were stabilized by adding 9 μl of BRB80T (BRB80 with 10 μM taxol). Biotinylated MTs were then coated with nQDs by adding 2 μl of streptavidin-coated nQDs (Quantum Dot Corp., Hayward, CA) to each sample, and incubating at room temperature with gentle shaking for 30 – 45 min. Both CdSe Qdot™ 585 (emission at 585 nm) and Qdot™ 605 (emission at 605nm) streptavidin conjugates were used in these experiments. The nQD-MT solutions were then brought to a final volume of 200 μl BRB80T. Images were collected with a CCD camera (Q-Fire, Olympus America Inc., Melville, NY or Orca II ER, Hamamatsu Corp., Bridgewater, NJ) and analyzed using AnalySIS (Soft Imaging Systems, Lakewood, CA).

A number of nQD-MT structures were assembled by random incorporation of biotinylated tubulin in MT filaments. Incorporation of as little as 6.25% biotinylated tubulin resulted in linear chains of nQDs along the length of MT filaments that were easily observable by fluorescence microscopy. At high concentrations of biotinylated

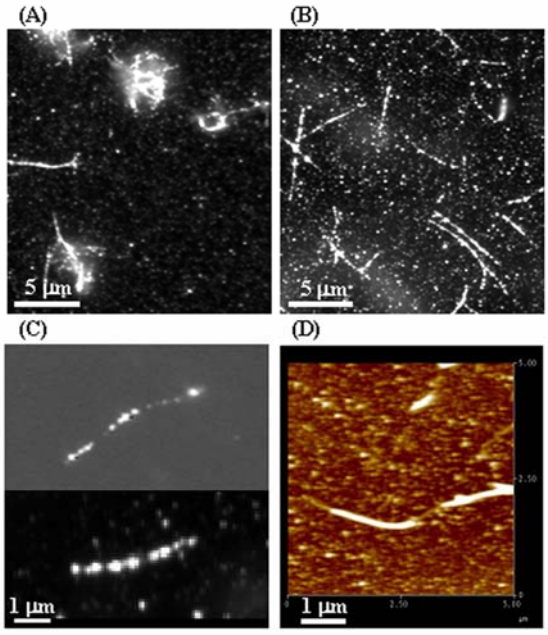

Figure 2.1. Fluorescence micrographs of CdSe nQD-MT structures formed at concentrations of 100% (A) and 25% (B) biotinylated tubulin. Clustering of nQDs within individual MTs was observed by fluorescence microscopy (C) and atomic force microscopy (D), independent of biotin concentration.

tubulin (i.e., 50 & 100%), assembly of nQD-MTs resulted in the formation of a variety of 3D aggregate structures (15 – 25 μm in size), mainly consisting of random, net-like formations (Fig. 2.1A). Interactions of a single nQD with multiple MT filaments are likely the basis for the assembly of these 3D structures. Such aggregate structures were not observed at concentrations less than 25% biotinylated tubulin. Further, the highest density of linear nQD chains was observed at a concentration of 25% biotin (Fig. 2.1B), and generally decreased as a function of decreasing concentrations of biotinylated tubulin. Clustering of nQDs within individual MTs was frequently observed (Fig. 2.1C), irrespective of the biotin concentration. In control experiments where no biotinylated tubulin was incorporated into the MT filaments, nQDs were randomly dispersed with no specific binding to the MTs.

Atomic force microscopy (AFM) and transmission electron microscopy (TEM) were used to further examine the dispersion of nQDs within individual MT filaments. For AFM experiments, nQD-MT assemblies were imaged in BRB80T buffer solution in tapping mode on a Digital Instruments Nanoscope IIIa Multimode scanning probe microscope with Olympus tips (nominal spring constants of 0.06 N m^{-1}). Freshly cleaved mica was incubated in the AFM fluid cell with a poly-l-lysine solution (1 mg/mL) for 30 min. The fluid cell was then flushed with buffer, and the poly-l-lysine-coated mica was imaged to establish a baseline. The MT solution (4 μM) was injected into the fluid cell and incubated for approximately 1 hr to allow reasonable MT surface coverage. The fluid cell was flushed with buffer again prior to imaging. TEM samples were prepared by adsorbing nQD-MTs to SiN grids (SPI Supplies, West Chester, PA) coated with

microtubule-associated proteins; TEM was performed using a Philips CM 30 TEM at 300 kV. AFM topographic imaging confirmed the observation of nQD clustering within individual MT filaments. Linear segments of uniformly coated nQDs were distinctly separated by shorter segments of uncoated tubulin (Fig. 1D). The average heights of the uncoated and nQD-coated regions of these MTs were approximately 16 and 32 nm, respectively, which agrees with the known size of each component. TEM images (*not shown*) also suggested that the dispersion of nQDs on MTs was relatively dense with small gaps between highly decorated regions. Overall, the results suggest that MTs "phase separate" in which the biotinylated tubulin tends to segregate in regions that are distinct from the biotin-free regions.

The observation of segmented nQD-loading on MTs motivated an alternate strategy (strategy 2) for assembling nQD-MTs in which centralized cargo-loading regions were formed within the MT structure. The underlying rationale of this strategy was to define specific regions within a MT for binding cargo, while leaving MT ends to free to interact with kinesin motor proteins. To assemble these structures, biotinylated MT "seeds" were initially formed, and then used to initiate polymerization of fluorescently labeled tubulin. The biotinylated seeds were assembled by suspending 20 μg biotinylated tubulin in 4 μl BRB80P, followed by polymerization for 90 sec at 37°C. These seeds were stabilized by adding 200 μl BRB80T, collected by centrifugation at 25,000 *x g* for 30 min, and resuspended in 4 μl BRB80P. Biotinylated seeds (1 μl) were then added to 20 μg of fluorescein isothiocyanate (FITC)-labeled tubulin that had been resuspended in 4 μl

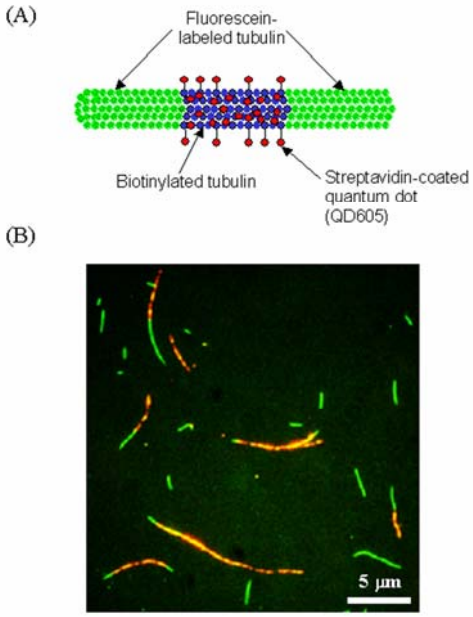

Figure 2.2. The structural composition of composite nQD-MT filaments formed with strategy 2. (A) Schematic illustration of a MT filament with a central biotinylated region with attached nQDs, surrounded by FITC-labeled tubulin. (B) Fluorescence micrograph showing the nQD-MT filaments composed of FITC-labeled tubulin (green) and nQD-coated region (red).

BRB80P. Following polymerization at 37°C for 20 min, the composite FITC-biotin MTs were stabilized by adding 8 μl BRB80T, followed by the addition of 2 μl of streptavidin-coated nQDs to coat the cargo-binding region. The MT-nQD solutions were incubated at room temperature with gentle shaking for 30 – 45 min, and then brought to a final volume of 250 μl. nQD-MT assemblies were then viewed by fluorescence microscopy; images were collected and analyzed as described above.

The resulting nQD-MT assemblies were composed of a central biotinylated core (with attached streptavidin-nQDs) surrounded by FITC-labeled tubulin (Fig. 2.2A). The nQD-MT-coated regions varied from <0.5 to 15 μm in length, with FITC ends ranging from <0.5 to 5 μm (Fig. 2.2B). The polarity of the MT was easily noted based upon the unequal rate of polymerization from opposing ends of the biotinylated seeds. Further, a percentage of the MTs possessed only a single end composed of FITC-labeled tubulin, likely resulting from shearing of the MT filament post-polymerization. Compared with prior experiments, aggregate 3D nQD-MT structures were not observed with this polymerization scheme, despite the formation of MT seeds using 100% biotinylated tubulin. Overall, these composite nQD-MT assemblies demonstrate the ability to assemble and organize localized regions of nQDs. This strategy may be further adapted to forming a number of nQD-binding regions, each with a distinct attachment chemistry, which in turn would enable attachment of nQDs with different sizes and emission spectra.

2.4 Transport of nanocomposite assemblies

Inverted motility assays[17] were used to evaluate kinesin-based transport of the various nQD-MT structures. A full-length, histidine-tagged *Drosophila melanogaster* dimeric kinesin was expressed and purified from *Escherichia coli* as previously described[18]. Standard flow cells were constructed using a microscope slide, double-sided tape, and a #1 glass coverslip. A solution of casein (0.5 mg/mL in BRB80) was infused into a flow cell (5 minutes) followed by a solution of *Drosophila* kinesin (~5 nM in BRB80 + 0.2 mg/mL casein + 1 mM MgATP) for 5 minutes. The motility solution (40 nM nQD-MT in BRB80 + 0.2 mg/mL casein + 10 μm taxol + 1 mM MgATP) was then infused into the flow cell. nQD-MT transport was observed using an Olympus IX71and 100x oil-immersion lens; time-lapsed images were collected using a CCD camera. Binding affinity between kinesin and nQD-MT was estimated by counting the number of MTs in a given field of view (65 x 50 μm) and dividing by 3.25 to standardize the values in number of MT per 1,000 μm^2. Transport velocities were calculated by estimating the distance traveled by an nQD-MT following subtraction of sequential images. A minimum sample size of fifteen nQD-MTs was used to estimate velocities for each variation. Tetrarhodamine isothiocyanate (TRITC)-labeled MTs were used as a control for comparing the velocities of nQD-MTs. Analysis of variance on ranks was used to evaluate differences in transport velocities.

Although single chains of nQD-MTs were assembled through random incorporation of biotinylated tubulin (strategy 1), kinesin-driven transport of these nQD-MTs was significantly inhibited by the presence of nQDs. The presence of attached nQDs, even at biotinylated tubulin concentrations as low as 6.25%, decreased the kinesin-binding of MT by an order of magnitude (Fig. 2.3). As a whole, kinesin binding of nQD-MTs was significantly lower ($P < 0.001$) compared with control, TRITC-labeled MTs (Fig. 2.3). Further, nQD-MT binding by kinesin was not dependent on the biotinylated tubulin

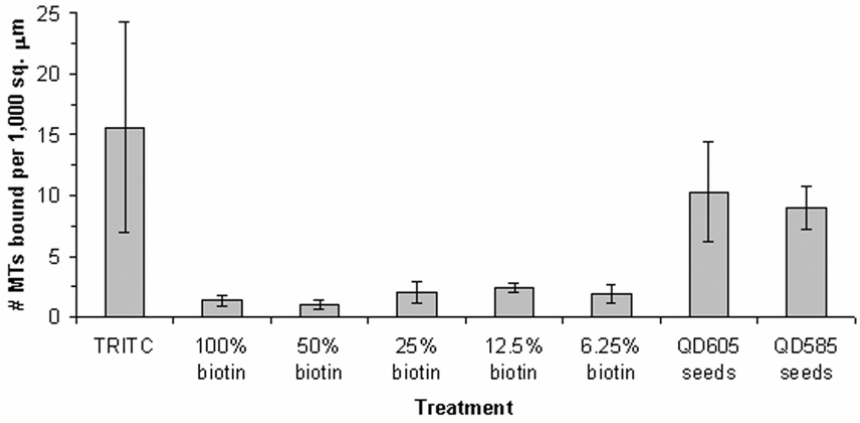

Figure 2.3. Comparison of the binding affinity of control (TRITC-labeled) and nQD-coated MTs as a function of varying biotinylated tubulin concentration (strategy 1) and structural composition (strategy 2). QD605 and QD585 seeds represent MTs in which the only the central region of the MT contained biotinylated tubulin and attached nQDs. Binding affinity was estimated by counting the number of MTs in a given field of view (65 x 50 μm) and dividing by 3.25 to standardize the values in number of MTs per 1,000 μm^2.

concentration, suggesting that the relative density of nQDs on a given MT was not a significant factor with respect to kinesin affinity. Three-dimensional aggregate structures were not observed bound by surface-tethered kinesin at any concentration of biotinylated tubulin. In addition to the reduction in nQD-MT binding, the relatively few bound nQD-MTs were unable to be transported by kinesin regardless of biotin concentration in the MT filament. Although rare, short segments of nQD-MTs were observed to move at biotin concentrations below 25%; linear translations of entire nQD-MTs was never observed. Based on these results, uniform functionalization of MT filaments with nQDs appears to block the necessary interactions required for both the binding and transport of MT by kinesin. Movement of MT segments suggests that nQD-coating of MTs sterically inhibits or eliminates fundamental interactions between the kinesin and MTs, compromising both shuttle adsorption and transport. Because kinesin contacts both the α and β tubulin subunits during transport[19,20], processive movement of kinesin is likely disrupted due to steric interference based on the relative size of the streptavidin-coated nQDs (~10-15 nm) with respect to tubulin dimers (~8 nm). The observation that portions of a given nQD-MT can be responsive at low biotin concentrations, however, suggests that modification of the MT structure may permit successful kinesin-based transport. Moreover, kinesin-based transport may potentially be maintained by changing the effective length and position of the linker, which in turn would increase the associated distance between the tubulin dimer and functionalized nQD, and may permit unaffected interaction between the kinesin motor domain and tubulin.

Inverted motility assays were subsequently performed to evaluate the kinesin-based binding and transport of nQD-MT composites formed using strategy 2 (i.e., MTs with a centrally defined nQD-binding region). The overall kinesin-based adsorption of these

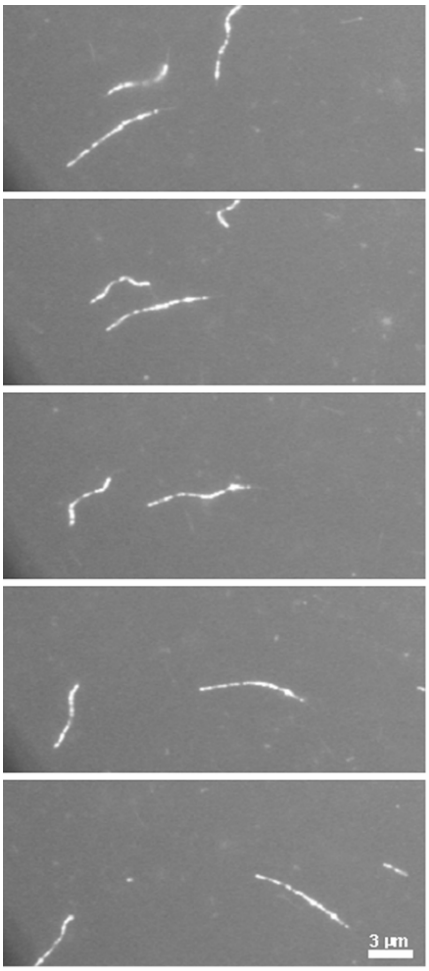

Figure 2.4. Time lapsed micrographs of kinesin-driven transport of nQD-MTs in which nQDs were localized to the central region of the MT filament. Images represent 10-sec time intervals.

nQD-MTs did not differ significantly compared to TRITC-labeled MTs (P = 0.254; Fig. 2.3), directly contrasting the results observed for MTs with randomly dispersed nQDs (strategy 1). Moreover, kinesin motor proteins were able to successfully transport these nQD-MTs in the inverted motility assays (Fig. 2.4). As expected for conventional kinesin, transport of nQD-MTs always occurred with the shorter, FITC-labeled tail (i.e., minus end) of the MT as the leading end. The translational velocities of centralized nQD-MTs (0.303 ± 0.008 μm/sec) did not differ significantly compared to control TRITC-labeled MTs (0.304 ± 0.013 μm/sec; P = 0.867). Together the data suggest that the ends of MT filaments are critical to both the binding and transport of nQD-coated MTs. Overall, these experiments demonstrate the ability to actively transport nanoscale photonic structures using kinesin motor proteins, and provide a fundamental mechanism for coupling nQDs to MTs without affecting the transport properties of the actuation system.

2.5 Conclusions

In summary, our results establish a platform for assembling microscale structures of CdSe nQDs using MT scaffolds, as well actively transporting these photonic structures using biomolecular motors. Although the ability to transport microscale cargo using MT shuttles has been previously reported[21], our work demonstrates the ability to exploit the polymer nature of the MT structure to assemble and organize nanoparticles into composite structures that subsequently can be actively transported at synthetic interfaces. This system will provide enabling technologies for developing composite nanomaterials that incorporate biomimetic processes for assembling and configuring base material components. In the future, the use of lithographically defined surfaces[10,22-26] will be explored as a mechanism for directing the transport of the nQD-MTs in microfluidic systems with the goal of regulating fluorescence resonance energy transfer events among nQDs of different sizes and emission spectra. Such a capability may permit the future integration of active and dynamic photonic materials in biocompatible materials and systems.

2.6 Acknowledgment

The authors thank T.J. Headley for technical assistance with transmission electron microscopy imaging of nQD-MTs, and J. Howard for generously providing the *Drosophila* kinesin expression clone. This work was partially supported by the Division of Materials Sciences and Engineering in the Department of Energy Office of Basic Energy Sciences, and Sandia's Laboratory Directed Research & Development Office.

2.7 References

(1) McMillan, R. *Nat. Mater.* **2003**, *2*, 214-215.
(2) Whitesides, G. M.; Grzybowski, B. *Science* **2002**, *295*, 2418-2419.
(3) Vale, R. D.; Milligan, R. A. *Science* **2000**, *288*, 88-95.
(4) Block, S. M. *Cell* **1998**, *93*, 5-8.
(5) Asbury, C. L.; Fehr, A. N.; Block, S. M. *Science* **2003**, *302*, 2130-2134.
(6) Yildiz, A.; Tomishige, M.; Vale, R. D.; Selvin, P. R. *Science* **2004**, *303*, 676-678.
(7) Surrey, T.; Nédélec, F.; Leibler, S.; Karsenti, E. *Science* **2001**, *292*, 1167-1171.
(8) Nédélec, F.; Surrey, T.; Maggs, A. C. *Phys. Rev. Lett.* **2001**, *86*, 3192-3195.
(9) Haimo, L.; Thaler, C. *BioEssays* **1994**, *16*, 727-733.
(10) Dennis, J. R.; Howard, J.; Vogel, V. *Nanotechnology* **1999**, *10*, 232-236.
(11) Limberis, L.; Stewart, R. J. *Nanotechnology* **2000**, *11*, 47-51.
(12) Bohm, K. J.; Stracke, R.; Muhlig, P.; Unger, E. *Nanotechnology* **2001**, *12*, 238-244.
(13) Boal, A. K.; Headley, T. J.; Tissot, R. G.; Bunker, B. C. *Adv. Funct. Mater.* **2004**, *14*, 19-24.
(14) Behrens, S.; Rahn, K.; Habicht, W.; Bohm, K.; Rosner, H.; Dinjus, E.; Unger, E. *Adv. Mater.* **2002**, *14*, 1621-1625.
(15) Fritzsche, W.; Kohler, J. M.; Bohm, K. J.; Unger, E.; Wagner, T.; Kirsch, R.; Mertig, M.; Pompe, W. *Nanotechnology* **1999**, *10*, 331-335.
(16) Fritzsche, W.; Bohm, K. J.; Unger, E.; Kohler, J. M. *Appl. Phys. Lett.* **1999**, *1*, 2854-2856.
(17) Howard, J.; Hunt, A.; Baek, S. *Meth. Cell Biol.* **1993**, *39*, 137-147.
(18) Coy, D. L.; Wagenbach, M.; Howard, J. *J. Biol. Chem.* **1999**, *274*, 3667-3671.

(19) Amos, L.; Hirose, K. *Curr. Opin. Cell Biol.* **1997**, *9*, 4-11.
(20) Hirose, K.; Lockhart, A.; Cross, R.; Amos, L. *Proc. Natl. Acad. Sci. USA* **1996**, *93*, 9539-9544.
(21) Hess, H.; Clemmens, J.; Qin, D.; Howard, J.; Vogel, V. *Nano Lett.* **2001**, *1*, 235-239.
(22) Clemmens, J.; Hess, H.; Howard, J.; Vogel, V. *Langmuir* **2003**, *19*, 1738-1744.
(23) Hiratsuka, Y.; Tada, T.; Oiwa, K.; Kanayama, T.; Uyeda, T. Q. P. *Biophys. J.* **2001**, *81*, 1555-1561.
(24) Hess, H.; Clemmens, J.; Matzke, C. M.; Bachand, G. D.; Bunker, B. C.; Vogel, V. *Appl. Phys. A* **2002**, *75*, 309-313.
(25) Clemmens, J.; Hess, H.; Lipscomb, R.; Hanein, Y.; Böhringer, K. F.; Matzke, C. M.; Bachand, G. D.; Bunker, B. C.; Vogel, V. *Langmuir* **2003**, *19*, 10967-10974.
(26) Hess, H.; Matzke, C. M.; Doot, R.; Clemmens, J.; Bachand, G. D.; Bunker, B. C.; Vogel, V. *Nano Lett.* **2003**, *3*, 1651-1655.

3.0 Physical factors affecting kinesin-based transport of synthetic nanoparticle cargo

Marlene Bachand, Amanda M. Trent, Bruce C. Bunker, and George D. Bachand

3.1 Abstract

Recently, kinesin biomolecular motors and microtubules filaments (MTs) were used to transport metal and semiconductor nanoparticles with the long-term goal of exploiting this active transport system to dynamically assemble nanostructured materials. In some cases, however, the presence of nanoparticle cargo on MTs was shown to inhibit transport by interfering with kinesin-MT interactions. The primary objectives of this work were (1) to determine what factors affect the ability of kinesin and MTs to transport nanoparticle cargo, and (2) to establish a functional parameter space in which kinesin and MTs can support unimpeded transport of nanoparticles and materials. Of the factors evaluated, nanoparticle density on a given MT was the most significant factor affecting kinesin-based transport of nanoparticles. The density of particles was controlled by limiting the number of available linkage sites (i.e., biotinylated tubulin), and/or the relative concentration of nanoparticles in solution. Nanoparticle size was also a significant factor affecting transport, and attributed to the ability of particles ≤40 nm in diameter to bind to the "underside" of the MT, and block kinesin transport. Overall, a generalized method of assembling and transporting a range of nanoparticle cargo using kinesin and MTs was established.

3.2 Introduction

The intrinsic properties of biological materials differ considerably from those of synthetic materials. Whereas synthetic materials are relatively static, living systems actively consume energy to assemble, reconfigure, and dismantle materials in a highly dynamic and non-equilibrium manner. These energy-driven processes enable biological materials to adapt to continuously changing environmental conditions and stimuli. Recently the ability to integrate biomolecular components and processes with synthetic nanoscale systems has been demonstrated,[27-30] and provides an impetus for developing dynamic and adaptive materials using active biological components. Exploiting and integrating such active assembly processes into nanocomposite materials opens the door to developing new classes of materials in which the assembly, configuration, and disassembly can be programmed or self-regulated. To this end, the overall goal of our work is to utilize active transport systems used by living systems to assemble, organize, and transport nanocomposite materials in microfluidic environments.

Kinesin motor proteins and microtubule filaments (MTs) represent one of Nature's elegant means for transporting nano- and molecular scale materials within a cell. This transport system plays a key role in a number of physiological processes such as mitosis,[31,32] as well as in response mechanisms such as the color changing ability of many fish.[9] Although kinesins can be grouped into a number of different subfamilies, the overall structure and morphology of all kinesins are relatively similar and include a motor domain, a neck-linker region, and in many cases an α-helical coiled-coil tail region. In all cases, the motor domain is responsible for ATP hydrolysis and translation along MT

filaments in an asymmetric hand-over-hand manner,[5,6] producing a relative force of 5 – 8 pN,[33-36] or 40 – 60 pN·nm of work per step, with an efficiency ~50%.[4,33]

Based on the overall dimensions and work output, kinesin is an ideal candidate for integration as a biomolecular actuator and transporter in hybrid nanodevices and materials. The stochastic nature of kinesin movement along MTs favors the use of the inverted motility geometry (Fig. 3.1) as a means of transporting nanoscale cargo over long distances. In this geometry, kinesins are adsorbed to synthetic surfaces, and propel MTs as "molecular shuttles" across a surface.[10] Work by Hess et al. demonstrated the ability to transport synthetic cargo on MT shuttles using streptavidin-coated microspheres attached to biotinylated MTs. [21,37] More recently, the ability to assemble streptavidin-coated nanocrystal quantum dots (nQDs) on biotinylated MTs was reported using two strategies: random incorporation of biotinylated tubulin, and defined localization of biotinylated tubulin[28,29]. Kinesin-based transport of nQD-MTs, however, was observed only in assemblies in which biotinylated tubulin was localized to a central region within the MT.[29] In contrast, gold nanoparticles (Au-NPs) assembled on MTs with random incorporation of biotinylated tubulin were successfully transported by kinesin and MT shuttles.[28] For both Au-NPs and nQDs, the nanoparticle-coated MTs were assembled before use in gliding motility assays, which may be problematic due to attachment of nanoparticles to the entire surface of the MTs, which in turn could inhibit kinesin interaction with the MT surface.

Based on these results, the goal of the current work was to develop a generalized strategy for transporting a wide array of nanoparticle cargo using the kinesin/MT active transport systems. The specific objectives were (1) to determine what factors affect the ability of kinesin and MTs to transport nanoparticle cargo, and (2) to establish a functional parameter space in which kinesin and MTs can support unimpeded transport of nanoparticles and materials. An alternative approach to that used in prior work was used (Fig. 3.1), and involved assembling nanoparticles on MTs subsequent to the attachment of the MTs to surface-tethered kinesin. This approach should localize nanoparticle assembly to the tops and sides of the MTs, and alleviate any potential steric inhibition of kinesin transport due to the presence of nanoparticle cargo.

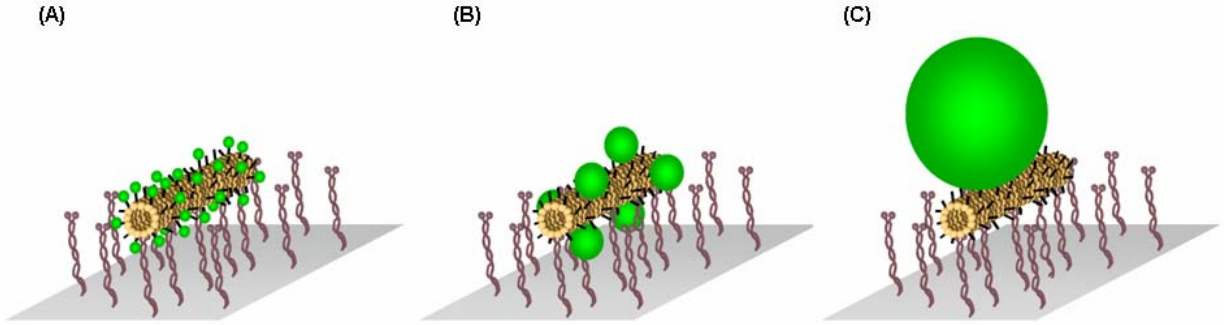

Figure 3.1. Schematic diagram of the protocol used to assemble and transport CdSe nQDs (**A**) and polystyrene microspheres (**B, C**) on MTs in the gliding motility assay.

3.3 Experimental details

For these experiments, varying degrees of biotinylated MTs were prepared by co-polymerizing biotinylated and tetramethylrhodamine isothiocyanate (TRITC)-labeled tubulin to obtain defined ratios (e.g., 6.25, 12.5, 25, 50 and 100% biotin). Polymerization was performed in BRB80 (80 mM Piperazine-1,4-bis(2-ethanesulfonic acid) (PIPES), 1 mM $MgCl_2$, 1 mM ethylene glycol-bis(2-aminoethylether)-N,N,N',N'-tetraacetic acid (EGTA), 1 mM GTP, and 10% glycerol at 37ºC for 20 min. Biotinylated MTs were subsequently stabilized with BRB80 and 10 μM taxol, and stored at room temperature. TRITC-labeled MTs (100%) were polymerized as described above, and served as a control. All experiments were conducted within 12 hrs after polymerization.

The inverted, gliding motility assay[17] was used to assemble and transport nanoparticles using MT scaffolds. A dimeric kinesin from *Drosophila melanogaster* was expressed and purified as previously described,[18] and used for all motility assays. Standard flow cells were constructed from a microscope slide, double-sided tape, and a #1 glass coverslip. A solution of casein (0.5 mg/mL in BRB80) was infused into a flow cell for 5 min, followed by a solution of *Drosophila* kinesin (50 mM imidazole, pH 7.0, 100 mM NaCl, 1 mM $MgCl_2$, 2 mM EGTA, 0.1 mM ethylenediaminetetraacetic acid, 5% sucrose (w/v), and 50 mM β-mercaptoethanol) for 5 min. A solution containing the biotinylated MTs in motility solution (BRB80, 0.2 mg/ml casein, 1 mM ATP, 10 μM taxol, 20 mM dextrose, 0.02 mg/ml glucose oxidase, 0.008 mg/ml catalase, and 0.5% β-mercaptoethanol) was then infused into the flow cell, and incubated for 5 min. Lastly, a solution of streptavidin-coated nanoparticles was infused into the flow cell, incubated for 2 – 15 min, and washed with 2 volumes of fresh motility solution (without nanoparticles).

Forty- and 1000-nm NeutrAvidin-coated yellow-green fluorescent (505/515) microspheres (1% solids, Molecular Probes Inc.) and QDot®525 streptavidin-conjugated nQDs (Quantum Dot Corp.) were used as nanoparticle-cargo in these experiments. These particles provided a range of sizes (i.e., ~15, 40, 1000 nm), as well as differing compositions (i.e., polystyrene versus CdSe). Dilutions of each nanoparticle type and size were prepared in motility solution in order to evaluate the effect of particle density on kinesin-based transport. The 1000-nm microspheres were diluted 1/250 (120 fM); the 40-nm microspheres were diluted at 1/500 (1 nM), 1/5,000 (100 pM), and 1/50,000 (10 pM). Streptavidin-coated nQDs were diluted 1/100 (10 nM) and 1/1,000 (1 nM).

All samples were examined by epifluorescence microscopy using an Olympus IX-71 inverted microscope and 100x oil immersion lens. Time-lapse images (1 sec intervals) were collected using a Hamamatsu Orca II-ER CCD camera, and subsequently processed using MicroSuite AnalySIS software (Soft Imaging Systems). Transport velocities were estimated by measuring the distance traveled by a MT (or particle) between subtracted images, and dividing by the time interval between images. Analysis of variance was used to determine statistical differences in transport velocity based on the percentage of biotinylated tubulin, particle size/type, and nanoparticle dilution.

3.4 Results & Discussion

Nanoparticle transport using MT shuttles

Transport of 1000-nm polystyrene spheres (120 fM concentration) was demonstrated using kinesin and MTs in the inverted motility geometry (Fig. 3.2a). In general, only a few 1000-nm spheres (i.e., 1-4) were attached to a given MT, and did not appear

dependent upon the percentage of biotinylated tubulin. Thus, the percent biotinylated tubulin and density of particles on a MT did not significantly affect transport velocity (p = 0.678; Table 3.1). The average transport velocity for biotinylated MTs carrying 1000-nm spheres was 0.53 μm/sec, and was consistent with control MTs without attached spheres. Based on the low viscous drag associated with an attached sphere (e.g., ~5 fN for a 1000-nm sphere) compared with force exerted by kinesin (5 pN/motor)[33-36], kinesin-driven transport of relatively large particles should be possible. For example, if we assume that surface-tethered kinesin interact with only a single protofilament in a given MT and are working in a concerted manner, a maximum of 125 kinesin are capable of binding per 1 μm of MT, resulting in a maximum net force of 625 pN (or ~62 pN per μm of MT if only a fraction (e.g., 10%) of the available sites are occupied by kinesin). By solving Navier-Stokes equation for the radius necessary to produce a drag force of 62 pN, a particle of ~12 mm in diameter would be required to completely stop the collective force of the kinesin and 1-μm MT. These calculations do not, however, account for additional factors such as increased drag due to the close proximity of the sphere to a boundary, or the increase in the apparent sphere weight as the overall size increases. Such factors would likely limit the maximum cargo size to substantially smaller spheres. Overall, our results agree with those reported by Hess et al.[21,37] for paramagnetic microspheres, and demonstrate the ability of MTs shuttles to transport considerably large cargo without affecting the speed and efficiency of transport.

Transport of 40-nm polystyrene spheres was supported by kinesin motors, and was significantly dependent on the density of particles attached to the MT shuttle. MTs were heavily coated with particles at 1 nM (1/500 dilution) and 100 pM (1/5,000 dilution), and remained attached to surfaces by kinesin; transport of these assemblies by kinesin, however, was significantly inhibited. Unimpeded transport of 40-nm particles was observed at the 10 pM dilution (1/50,000 dilution) of spheres, as shown in Fig. 3.2b. At this concentration, the percent biotinylation did not significantly affect the transport rate (p = 0.909; Table 1) of the 40-nm particles, despite a qualitatively observed difference in the number of particles attached to the MTs at the different degrees of biotinylation. These data suggest that cargo density is likely the dominating factor affecting transport of MTs and attached nanoparticle cargo. Kinesin-based transport is highly dependent upon unimpeded interaction between the motor protein and tubulin dimers. Thus, attachment of nanoparticles to the MTs at the specific region of kinesin interaction would significantly inhibit the transport. The total length of a kinesin motor is ~75 nm,[10] although neither the extent of the protein interaction with the surface nor the height of kinesin from the surface is known to any level of certainty. Based on the observed inhibition by these nanoparticles, our data suggest that the height above the surface is likely >40 nm, thus allowing nanoparticles to bind to the "underside" of the MT. Therefore, it is critical to control the density of nanoparticles in this size regime in order to mitigate potential steric interference between kinesin and MTs, and inhibition of MT transport.

nQDs were successfully transported using biotinylated MTs formed through random incorporation of biotinylated tubulin (Fig. 3.2c), in contrast to the previous report.[29] As observed with the higher concentrations of 40-nm spheres (i.e., >10 pM), MTs heavily coated with nQDs were observed at the 10 nM concentration (1/100 dilution), but unable to support kinesin-based transport. Transport of nQD-coated MTs was observed at the 1 nM concentration (1/1,000 dilution) of nQDs, and the transport velocity of the nQD-

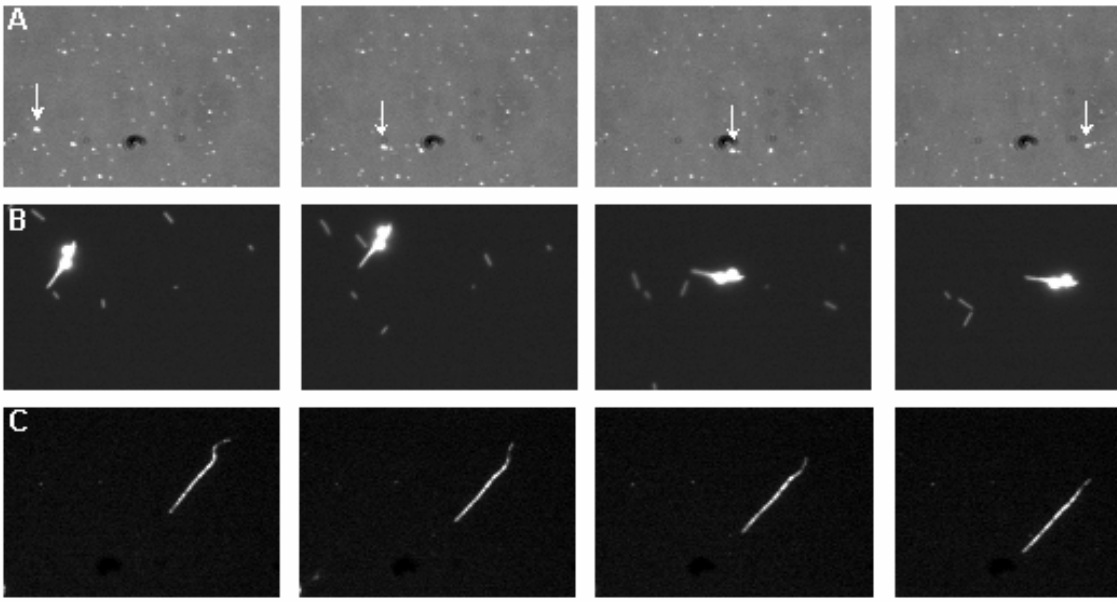

Figure 3.2. Time-lapse images of kinesin-based transport of 40- (**A**) and 1000-nm polystyrene spheres (**B**), and CdSe nQDs (**C**) on MT filaments. Interval between images = 10 sec; scale bar = 2 μm.

coated MTs displayed a significant dependency on the degree of biotinylated tubulin ($p < 0.001$). Differences in the relative density of nQDs attached to MTs as a function of biotinylated tubulin were qualitatively observed (*not shown*), and were consistent with the observed differences in transport velocity. For example, 100% biotinylated MTs displayed a much greater coating of nQDs and decreased transport velocity as compared with 6.25% biotinylated MTs. Further, transport velocities were significantly less for MTs with 100, 50, and 25% biotinylated tubulin at a 10 nM concentration of nQDs as compared with control TRITC-labeled MTs.

Overall, the results for both the 40-nm polystyrene spheres and ~15-nm nQDs suggest that the nanoparticle density on MTs is the most significant factor affecting kinesin-based transport of nanoparticles and MTs. Cargo density, in turn, is dependent upon both the percent biotinylated tubulin (i.e., available binding sites for particles), and the relative concentration of particles (i.e., relative number of particles available for attachment to MTs). Thus, kinesin-based transport of nanoparticles should be achievable by controlling one or both of these factors. The ability to transport polystyrene spheres, gold nanoparticles, and nQDs of differing sizes using kinesin and MTs has been demonstrated,[28,29] which suggests that particle composition is not a significant factor affecting transport. Nanoparticle size, however, can be a significant factor as particles ≤40 nm are capable of binding to the "underside" of the MT, and can block the interactions between kinesin and MTs that are necessary for transport. Our data also suggest that particle size influences the relative concentration of nanoparticles at which kinesin-based transport occurs. For example, a significantly greater concentration of 15-nm nQDs could be transported on the MT shuttles as compared with 40-nm polystyrene spheres (i.e., 10 nM versus 10 pM, respectively; Table 3.1). Thus, this relationship

Table 3.1. Mean transport velocities (μm/sec) of 40 and 1000-nm polystyrene (PS) spheres and 15-nm CdSe nQDs attached to MT shuttles as a function of nanoparticle concentrations and biotinylated tubulin.

		Percent Biotinylated Tubulin				
	Control	100%	50%	25%	12.5%	6.25%
1000-nm PS spheres						
120 fM	0.52 (0.04)[b]	0.56 (0.05)	0.55 (0.05)	0.51 (0.03)	0.51 (0.03)	0.53 (0.05)
40-nm PS spheres						
1 nM	0.55 (0.02)	NT[a]	NT	NT	NT	NT
100 pM	0.55 (0.02)	NT	NT	NT	NT	NT
10 pM	0.55 (0.02)	0.55 (0.02)	0.55 (0.02)	0.56 (0.03)	0.56 (0.04)	0.54 (0.02)
15-nm nQDs						
10 nM	0.58 (0.03)	NT	NT	NT	NT	NT
1 nM	0.58 (0.03)	0.34 (0.04)	0.49 (0.04)	0.48 (0.05)	0.55 (0.06)	0.58 (0.03)

[a] NT = no transport observed.
[b] 2SE (2 * standard error of the mean)

between particle size and concentration must be considered in terms of optimizing the conditions necessary to kinesin transport of nanoparticle cargo.

Interactions between nanoparticle-coated MTs

Several types of interactions between nanoparticle-coated MTs were observed for nQDs and 1000-nm polystyrene spheres during kinesin transport. Transfer of 1000-nm spheres from one MT to another MT was observed when cargo-carrying MTs collided with MTs lacking an attached sphere. More commonly, collisions between MTs with and without spheres resulted in the formation of aggregates, with the sphere serving as the "glue." In other cases, MTs moved in a circular pattern, which often resulted in the attached sphere binding separate sections of the MT, and forming a circular structure capable of being transported by kinesin (Fig. 3.3a). Such circular structures were also observed for nQD-coated MTs (Fig. 3.3b), and led to the formation of larger aggregated circular structures (Fig. 3.3c). In all cases, these circular structures were capable of being transported by kinesin despite the aggregation of MTs.

The formation of these circular structures appears dependent on the attachment of nanoparticles to the MTs. The curved motion of cargo-carrying MTs in these experiments

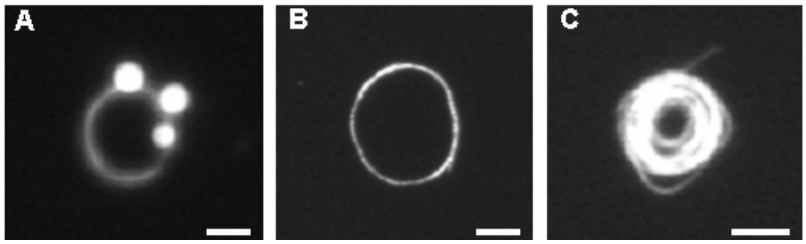

Figure 3.3. Circular, aggregate assemblies formed by MTs coated with 1000-nm polystyrene spheres (**A)** and CdSe nQDs (**B, C**). In all cases, kinesin-based transport of these assemblies remains viable. Scale bar = 2 μm.

may be due to the biased loading of nanoparticles to the tops and sides of the MTs, which in turn may have induced strain buildup in the MT. This curved motion eventually enables attached spheres to bind to an adjacent portion of the MT, and the formation of a circular structure. Further, large circular aggregates of nanoparticles and MTs resulted from collisions between free MTs and these circular MT structures, as shown in Fig. 3.4. In this example, the transport velocity of the nQD-coated MT (50% biotinylated tubulin) being incorporated into these circular aggregates was approximately 0.51 μm/sec, consistent with the velocity observed for non-aggregated MTs. Based on the diameter of this aggregate structure (i.e., ~6.3 μm), the rotation velocity of this structure was ~0.03 rps. Analysis of these circular aggregate structures showed a minimum interior radius of 0.85 μm, which is close to the radius at which MT breakage should occur (i.e., ~0.6 μm).[38]

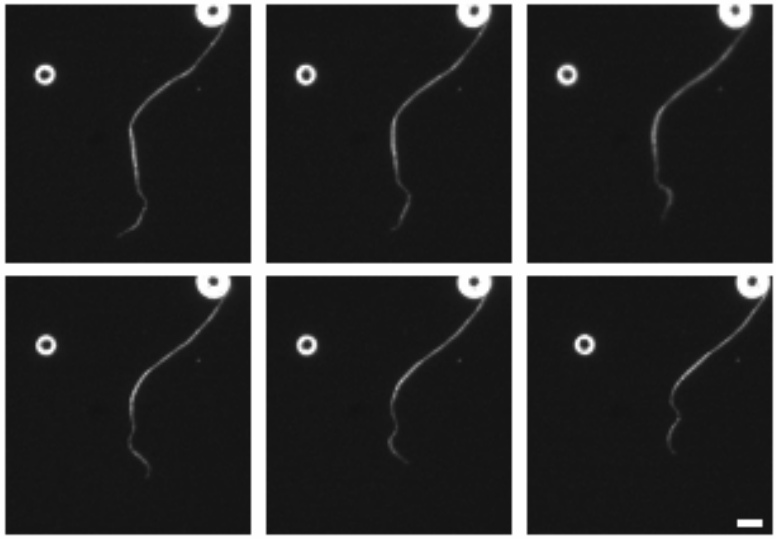

Figure 3.4. Time-lapse images showing two circular nQD-MT aggregate assemblies, and the kinesin-based transport of an nQD-coated MT as it becomes incorporated into the assembly in the upper right corner of the images. Time interval between images = 6 sec; scale bar = 5 μm.

Aggregate nQD-MT structures were not observed in prior work,[28,29] and may be attributed to the strategy for coating MTs. In previous reports, solutions of polymerized tubulin and nanoparticles were mixed prior to gliding motility assays, which likely results in unpolymerized biotinylated tubulin occupying some percentage of the streptavidin sites on the nanoparticles. Thus, collisions between MTs are less likely to result in the formation of aggregate structures based on the high occupancy of the streptavidin binding sites. In the current work, residual unpolymerized tubulin was removed from the flow cells by infusion of the nanoparticle solution, thus leaving more available biotin-binding sites on each nanoparticle. The observed aggregation may be lessened by pre-conditioning nanoparticles with biotin prior to attachment to MTs, or washing the nanoparticles following attachment to MTs with motility solution containing biotin. Alternatively, interactions between nanoparticle-carrying MTs may be used to assemble multicomponent structures if the interactions can be defined and controlled.

3.5 Conclusions

The present study demonstrates the ability of kinesin biomolecular motors and MT shuttles to transport nanoparticles with varying size, composition, and density. Linkage of nanoparticles to MTs shuttles was accomplished using biotin-streptavidin, forming a relatively strong, but non-covalent bond between components.[39] Nanoparticles were assembled on MTs that were bound to surface-tethered kinesin in order to avoid inhibition of transport as previously reported,[29] by localizing the attached cargo to the top and sides of the MT shuttles. The density of nanoparticles attached to MTs was the most significant factor affecting kinesin transport, and can be regulated by controlling the frequency of biotinylated tubulin, and/or the concentration of nanoparticles used for attachment. Nanoparticle size also impacted kinesin-based transport, as nanoparticles less than 40 nm in diameter are small enough to bind to the "underside" of the MT and block kinesin movement. Overall, the unimpeded transport of nanoparticles represents a first step to integrating active transport and assembly systems for developing dynamic and adaptive nanomaterials. Coupling nanoparticle transport with demonstrated methods of guiding MT transport[22,23,25,26,40] should provide a platform for directed, energy-driven transport of nanoparticles and materials at synthetic interfaces.

3.6 Acknowledgment

This work was partially supported by the Division of Materials Sciences and Engineering in the Department of Energy Office of Basic Energy Sciences, and Sandia's Laboratory Directed Research.

3.7 References

(1) McMillan, R. *Nat. Mater.* **2003**, *2*, 214.
(2) Whitesides, G. M.; Grzybowski, B. *Science* **2002**, *295*, 2418.
(3) Vale, R. D.; Milligan, R. A. *Science* **2000**, *288*, 88.
(4) Block, S. M. *Cell* **1998**, *93*, 5.
(5) Asbury, C. L.; Fehr, A. N.; Block, S. M. *Science* **2003**, *302*, 2130.
(6) Yildiz, A.; Tomishige, M.; Vale, R. D.; Selvin, P. R. *Science* **2004**, *303*, 676.
(7) Surrey, T.; Nédélec, F.; Leibler, S.; Karsenti, E. *Science* **2001**, *292*, 1167.
(8) Nédélec, F.; Surrey, T.; Maggs, A. C. *Phys. Rev. Lett.* **2001**, *86*, 3192.
(9) Haimo, L.; Thaler, C. *BioEssays* **1994**, *16*, 727.

(10) Dennis, J. R.; Howard, J.; Vogel, V. *Nanotechnology* **1999**, *10*, 232.
(11) Limberis, L.; Stewart, R. J. *Nanotechnology* **2000**, *11*, 47.
(12) Bohm, K. J.; Stracke, R.; Muhlig, P.; Unger, E. *Nanotechnology* **2001**, *12*, 238.
(13) Boal, A. K.; Headley, T. J.; Tissot, R. G.; Bunker, B. C. *Adv. Funct. Mater.* **2004**, *14*, 19.
(14) Behrens, S.; Rahn, K.; Habicht, W.; Bohm, K.; Rosner, H.; Dinjus, E.; Unger, E. *Adv. Mater.* **2002**, *14*, 1621.
(15) Fritzsche, W.; Kohler, J. M.; Bohm, K. J.; Unger, E.; Wagner, T.; Kirsch, R.; Mertig, M.; Pompe, W. *Nanotechnology* **1999**, *10*, 331.
(16) Fritzsche, W.; Bohm, K. J.; Unger, E.; Kohler, J. M. *Appl. Phys. Lett.* **1999**, *1*, 2854.
(17) Howard, J.; Hunt, A.; Baek, S. *Methods Cell Biol.* **1993**, *39*, 137.
(18) Coy, D. L.; Wagenbach, M.; Howard, J. *J. Biol. Chem.* **1999**, *274*, 3667.
(19) Amos, L.; Hirose, K. *Curr. Opin. Cell Biol.* **1997**, *9*, 4.
(20) Hirose, K.; Lockhart, A.; Cross, R.; Amos, L. *Proc. Natl. Acad. Sci. USA* **1996**, *93*, 9539.
(21) Hess, H.; Clemmens, J.; Qin, D.; Howard, J.; Vogel, V. *Nano Lett.* **2001**, *1*, 235.
(22) Clemmens, J.; Hess, H.; Howard, J.; Vogel, V. *Langmuir* **2003**, *19*, 1738.
(23) Hiratsuka, Y.; Tada, T.; Oiwa, K.; Kanayama, T.; Uyeda, T. Q. P. *Biophys. J.* **2001**, *81*, 1555.
(24) Hess, H.; Clemmens, J.; Matzke, C. M.; Bachand, G. D.; Bunker, B. C.; Vogel, V. *Appl. Phys. A* **2002**, *75*, 309.
(25) Clemmens, J.; Hess, H.; Lipscomb, R.; Hanein, Y.; Böhringer, K. F.; Matzke, C. M.; Bachand, G. D.; Bunker, B. C.; Vogel, V. *Langmuir* **2003**, *19*, 10967.
(26) Hess, H.; Matzke, C. M.; Doot, R.; Clemmens, J.; Bachand, G. D.; Bunker, B. C.; Vogel, V. *Nano Lett.* **2003**, *3*, 1651.
(27) Montemagno, C.; Bachand, G. *Nanotechnology* **1999**, *10*, 225.
(28) Bachand, G. D.; Rivera, S. B.; Boal, A. K.; Bauer, J. P.; Koch, S. J.; Manginell, R. P.; Liu, J.; Bunker, B. C. In *Materials Research Society Symposium Proceedings: Micro- and Nanosystems*; LaVan, D. A., Ayon, A. A., Madou, M. J., McNie, M. E., Prasad, S. V., Eds.; Materials Research Society, Warrendale, PA: Boston, MA, 2004; Vol. 782, pp A1.1.1.
(29) Bachand, G. D.; Rivera, S. B.; Boal, A. K.; Gaudioso, J.; Liu, J.; Bunker, B. C. *Nano Lett.* **2004**, *4*, 817.
(30) Soong, R.; Bachand, G.; Neves, H.; Olkhovets, A.; Craighead, H.; Montemagno, C. *Science* **2000**, *290*, 1555.
(31) Vale, R. D. *Trends Biochem.Sci.* **1999**, *24*, M38.
(32) Steinberg, G. *Trends Microbiol.* **2000**, *8*, 162.
(33) Kawaguchi, K.; Ishiwata, S. *Biochem. Biophys. Res. Commun.* **2000**, *16*, 895.
(34) Block, S. M.; Goldstein, L. G.; Schnapp, B. J. *Nature* **1990**, *348*, 348.
(35) Svoboda, K.; Schmidt, C. F.; Schnapp, B. J.; Block, S. M. *Nature* **1993**, *365*, 721.
(36) Hunt, A. J.; Gittes, F.; Howard, J. *Biophys. J.* **1994**, *67*, 766.
(37) Hess, H.; Howard, J.; Vogel, V. *Nano Lett.* **2002**, *2*, 1113.
(38) Waterman-Storer, C. M.; Salmon, E. D. *J. Cell Biol.* **1997**, *139*, 417.
(39) Lo, Y. S.; Simons, J.; Beebe, T. P. *J. Phys. Chem. B* **2002**, *106*, 9847.

(40) Clemmens, J.; Hess, H.; Doot, R.; Matzke, C. M.; Bachand, G. D.; Vogel, V. *Lab Chip* **2004**, 4, 83.

4.0 Interactions between cargo-carrying bio-molecular shuttles

Andrew K. Boal, George D. Bachand, Susan B. Rivera, and Bruce C. Bunker

4.1 Abstract

Microtubule shuttles propelled by the motor protein kinesin embedded in self-assembled monolayers are being developed for active transport functions in artificial microfluidic systems. As a model system, biotinylated microtubules have been laden with streptavidin-coated particles as cargo. The behavior of cargo-laden microtubules has been observed using fluorescence microscopy upon activation of kinesin-driven transport processes. Collisions between mobile microtubules and their particulate cargo result in six distinct behaviors: bypass, microtubule bending, particle dislodgement, particle transfers between microtubules, co-joining of microtubules to a common particle, and particle-induced severing of microtubules. The distribution of observed events can be described qualitatively based on the mechanics of motor proteins and microtubules, the geometry of the collision events, and the loading rate dependence of the strength of microtubule-particle binding. Implication of the results on the use of motor proteins in active transport and cargo handling systems for nanomaterials are described.

4.2 Introduction

Nature commonly employs energy consuming motor proteins for active transport and assembly functions including vesicle transport, cell division, cellular motility, and muscle actuation.[1] These processes allow for the fabrication and actuation of complex non-equilibrium structures that cannot be achieved from thermodynamically limited self-assembly processes.[2] Several research groups are currently investigating the extent to which active proteins can be exploited to transport, assemble, and actuate nanomaterials in artificial environments. Potential applications for active transport include the assembly, healing, and repair of nanomaterials, the reconfiguration of quantum dot arrays as optical sensor elements, and the active transport of analytes in microfluidic systems.

The specific active transport system that is the focus of this paper consists of the dyad formed between microtubules and the motor protein kinesin.[3] Microtubules are 25 nm diameter cytoskeletal filaments ranging in length from 1-1000 μm that are formed by the polymerization of the protein tubulin. In cells, the microtubules constitute the transportation network along which motor proteins such as kinesin move. Kinesin has a foot-like motor domain that binds to microtubules and processively takes 8 nm steps along the microtubule by converting the chemical energy obtained by the hydrolysis of 5'-adenosine triphosphate (ATP) into physical movement.[4] Kinesin also has a long tail that is terminated by a binding region used to transport intracellular cargo such as vesicles, or manipulate chromosomes during mitosis.[5]

Transport in living systems is provided when kinesin "walks" along microtubules to carry cargo to desired locations. For extra-cellular environments, we have been exploring an inverted geometry for achieving active transport[6,7] of nanoparticles such as quantum dots[8] (Fig. 4.1). In this case, the kinesin tail is used to attach the molecular motor to

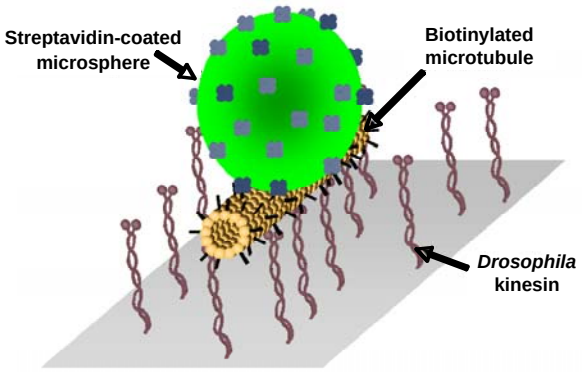

Figure 4.1. Illustration of the inverted geometry used for the transport of streptavidin-coated cargo by biotin-functionalized microtubules across a kinesin surface.

substrate surfaces within self-assembled monolayers rather than to carry cargo. Short segments (2-10 μm) of taxol-stabilized microtubules are then adsorbed by the kinesin-containing surfaces. In the presence of ATP, the microtubule shuttles are propelled across the substrate surface by many tethered motors. The microtubules can be functionalized to interact with other species such as nanoparticles. Ultimately, we are interested in creating microsystems in which mobile microtubules pick up such cargo, transport the cargo to desired locations, and then deposit and assemble the transported objects into desired structures. Performing such active transport functions will require controlling the interactions between microtubules, cargo, and both loading and unloading stations.

To help develop design rules for active motor protein transport, we have investigated the behavior of a model system in which particles are attached to microtubules using passive biotin-streptavidin linkages[9] (Fig. 4.1). The biotin-streptavidin linkage has been successfully applied in the kinesin-microtubule system for the transport of polymer beads,[10] CdSe quantum dots,[8] gold nanoparticles, and DNA molecules.[11] In all cases, biotin-functionalized microtubules have been used to bind streptavidin-coated cargos. Given the well-known strength ($K_a = 10^{15}$ M^{-1}) of biotin binding to streptavidin[12] and the well-characterized loading-rate dependent bond rupture force between the two components (5 pN to over 1000 pN)[13], the biotin-streptavidin linkage provides an ideal starting point for studying interactions between components in active transport systems. In previous work,[14] a single collision event between a surface-immobilized biotinylated microtubule and a kinesin-propelled biotinylated microtubule carrying a streptavidin-coated polymer bead was observed to result in the transfer of the bead from a mobile to an immobile microtubule. The force necessary to affect this transfer was estimated to be on the order of 5 pN. Such results clearly illustrate that microtubules can be used for cargo transfer functions within microfluidic systems. However, the results do not provide much information regarding the probability of such cargo transfer events, or the identity of the primary factors that mediate cargo loading, transport, and unloading functions. To elucidate cargo-handling behavior, we have performed a series of experiments in which mobile biotinylated microtubules carrying streptavidin-coated polystyrene beads are

allowed to collide with and interact with other mobile microtubules. Both beads and microtubules were optically tagged (with Dragon Green dye, and rhodamine, respectively) to allow component behavior to be monitored using fluorescence microscopy. Results were obtained at both 24°C and 30°C, as heating is known to decrease the force required to break biotin-avidin interactions,[15] as well as increase the speed at which kinesin propels microtubules.[16] By analyzing what happens as a result of these collisions, we have identified several key parameters that ultimately must be controlled to optimize active transport systems based on motor proteins.

4.3 Experimental

Recombinant *Drosophila melanogaster* dimeric kinesin bearing a C-terminus polyhistidine tag was purified from an overproducing strain of *E. coli* by Ni^{2+} chromatography as previously described.[17] Rhodamine- and biotin-labeled tubulin were purchased and used as received from Cytoskeleton, Inc. Streptavidin-coated polystyrene beads (0.56 μm diameter, tagged with Dragon Green dye (excitation at 480 nm, emission at 520 nm)) were purchased as a 1% solids solution from Bangs Laboratories, Inc. All other reagents were purchased and used as received from Sigma/Aldrich Chemical Co.

Microtubules were prepared by polymerizing a 90:10 mass ratio mixture of rhodamine:biotin tubulin at a concentration of 5 mg/mL in BRB80-P (80 mM PIPES, 1 mM EGTA, 1 mM $MgCl_2$, 1 mM GTP and 10% glycerol, pH 6.9) for 20 min at 37˚C. The resulting microtubule solution was then stabilized with taxol by the addition of BRB80-T (80 mM PIPES, 1 mM $MgCl_2$, 1mM EGTA, 2μm taxol, pH 6.9) to give a final protein concentration of 50 μg/mL. These solutions were used within 24 hours of preparation.

Microscope flow cells were fabricated by attaching a 25 mm x 25 mm #1 cover slip to a 3” x 1” microscope slide with two pieces of double-sided tape ~5 mm apart so as to form a channel with a capacity of ~15 μL. A 20 μL aliquot of BRB80-CS0.5 (80 mM PIPES, 1 mM $MgCl_2$, 1mM EGTA, 0.5 mg/mL casein, pH 6.9) was flowed into the cell and incubated for 5 minutes. Next, a 15 μL aliquot of BRB80-K (80 mM PIPES, 1 mM $MgCl_2$, 1mM EGTA, 1 mM Na_2ATP, 0.2 mg/mL casein, 0.1 mg/mL kinesin, pH 6.9) was flowed into the cell followed by another five minute incubation. Finally, a mixture of microtubule-motility (80 μL BRB80-CS0.5 with 2 μM taxol, 1 μL 2M dextrose, 1 μL 100 mM MgATP, 1 μL 0.8 mg/mL catalase, 1 μL 2 mg/mL glucose oxidase, 0.5 μL 2-mercaptoethanol, 20 μL 80 μg/mL microtubule solution, pH 6.9) and particle-motility (90 μL BRB80-CS0.5 with 2 μM taxol, 1 μL 2M dextrose, 1 μL 100 mM MgATP, 1 μL 0.8 mg/mL catalase, 1 μL 2 mg/mL glucose oxidase, 0.5 μL 2-mercaptoethanol, 10 μL streptavidin-coated beads solution, pH 6.9) solutions were added into the flow cell. A 3:7 volume ratio of the two solutions was selected for all experiments, as this ratio was observed to achieve the maximum number of microtubules bound to the kinesin surface and bearing single particles. Solution concentrations of microtubules and beads were typically adjusted to provide approximately 100 microtubules in the microscope field of view, of which 5 or so were carrying a bead. These conditions resulted in a prevalence of collision events between microtubules carrying single particles, simplifying the observation and classification of collision events. Experiments were performed at 30˚C by heating with both a calibrated Peltier heater from the bottom and a heated oil-

immersion objective from the top. Samples were allowed to thermally equilibrate for 15 minutes before data was acquired.

Fluorescence microscopy was performed on an Olympus BX51 inverted microscope using a 100x oil immersion objective. Images were recorded using a Hamamatsu C4742-98 digital camera and processed using the MicroSuite software package. Microscopy data was acquired by taking movies at a rate of one second per frame over a five minute period. Analysis of collision events was accomplished by reviewing all movies for a given biotin concentration. This process involved analysis of at least 12 videos involving 150 to 325 clearly observable collision events for each sample.

4.4 Results

Collisions between bead-carrying and bead-free microtubules give six distinct outcomes (Fig. 4.2): 1) Bypass – Microtubules cross over each other with minimal distortion or deflection. 2) Microtubule Bending – The bead-free tube is bent as it collides with the bead on the other microtubule, but does not appear to slow down or stick to the bead. 3) Particle Dislodgement – The stress imposed by the bead-free microtubule can be sufficient to dislodge the bead from the parent microtubule (like a "nano-slingshot"), resulting in a free particle that is bound to neither microtubule. 4) Particle Transfer – The bead-free microtubule can bind to the particle, resulting in a hand-off of the bead from the host to the encountered microtubule. 5) Microtubule Joining – When both microtubules interact strongly with the particle, the particle can glue the microtubules together, forcing one microtubule to tag along with the other. 6) Microtubule Severing – In rare cases, the bead-free microtubule is severed when it collides with a bead being transported by another microtubule.

The distribution of the collision outcomes listed above was measured at both 24^{o}C and 30^{o}C. For each temperature, at least 150 clearly observable collisions were observed and assigned to one of the six distinct categories. Regardless of temperature (Fig. 4.3), collisions resulted in non-interactive bypass events 45-55% of the time. At room temperature, the next most probable events were microtubule joining and bending (15-20% each), followed by particle transfers (10-15%). Particle knock-off and microtubule severing events were relatively rare (around 5% and 1%, respectively). The same general trends were observed at 30^{o}C. However, particle transfer events were only half as prevalent at 30^{o}C than at 24^{o}C.

4.5 Discussion

In order to design optimized active transport systems, we need to be able to understand and manipulate the key factors controlling the distribution of collision events involving microtubule shuttles with other shuttles and channel walls. Our model system of biotinylated microtubules and streptavidin-coated polystyrene beads provides a framework against which models for component interactions can be evaluated. The observed distributions can be rationalized on the basis of the mechanics of motor proteins, the biotin-streptavidin linkage, and the microtubules themselves. The motor proteins determine the velocities and forces applied to the colliding objects. Our kinesin moves at a velocity of 0.4 μm/sec[16], with a force per motor of 5 pN.[3] The collective force applied by a typical motor protein monolayer (3600 kinesin/μm^2) on a typical microtubule (5 μm long) can be substantial (up to 1500 pN if all motors are working in concert). The biotin-streptavidin linkage determines whether components are joined

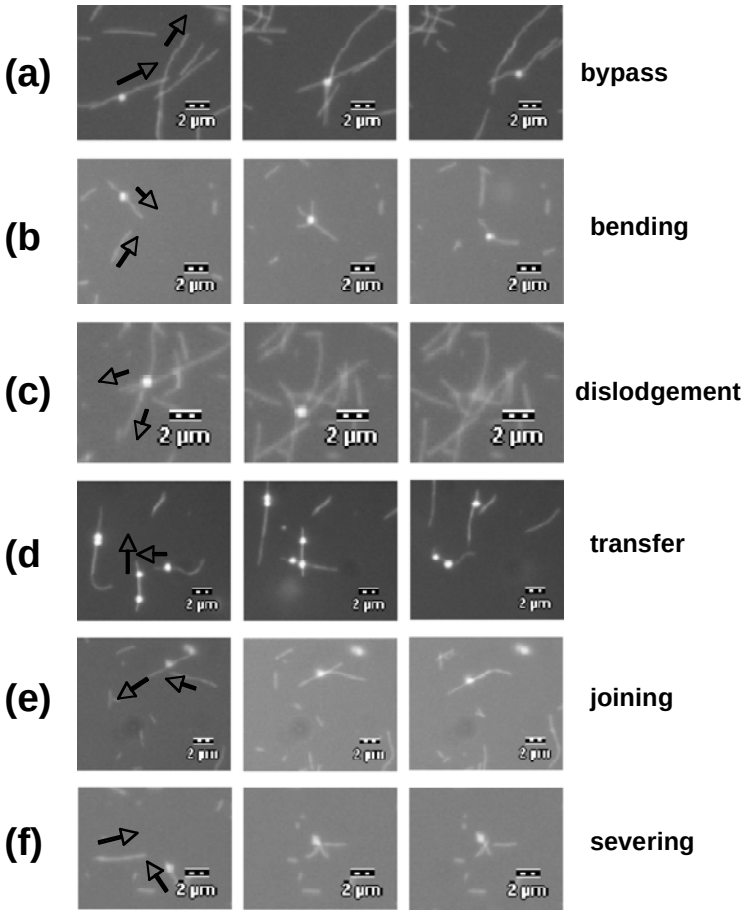

Figure 4.2. Fluorescent micrographs taken from sequences showing the various outcomes of a particle-laden microtubules colliding with a particle-free microtubule. (See Web site for complete video sequences.) Events shown are: a) bypass, b) microtubule bending, c) bead knock-off, d) bead transfer, e) microtubule joining, and f) microtubule severing. In all cases, black arrows indicate the initial direction of microtubule motions, with times given relative to the left image of each sequence (corresponding to t = 0). The scale bars for each sequence are shown. Times between frames are a minimum of one second (e.g. for frames 2 and 3 in c)), but times between frames in most sequences are arbitrary, as sequences were selected to illustrate behaviors rather than kinetics. When important for analyses, time intervals are indicated in the text.

together in encounters or if component linkages fail under the stresses associated with a particular collision. The force required to rupture the biotin-streptavidin linkage is a dynamic property that is proportional to the logarithm of the loading rate[13] (e.g. 25 pN and 500 pN at loading rates of 1 pN/s and 7.5 x10^4 pN/s, respectively) and inversely proportional to temperature.[15] Therefore, the outcome of a given collision can be dictated by the loading rates that are experienced.

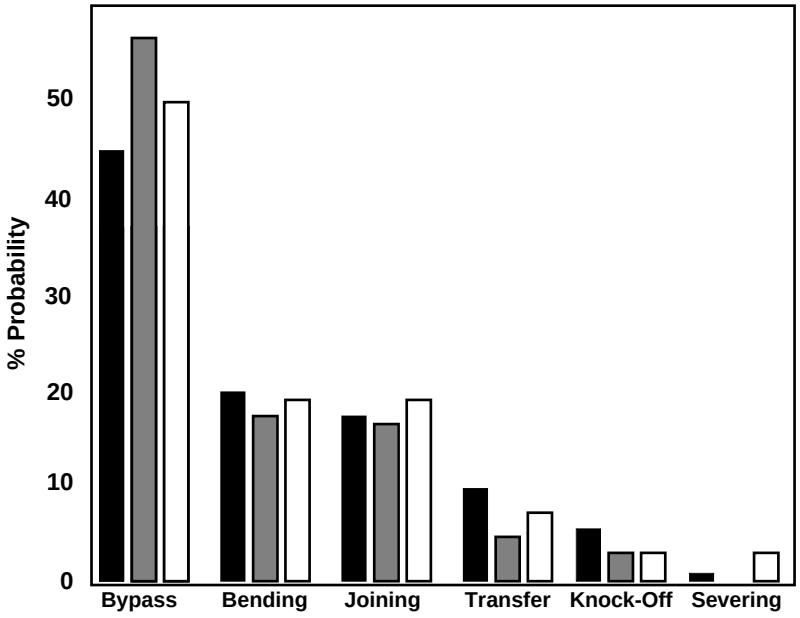

Figure 4.3. Bar graphs showing the percentage of collision events exhibiting the indicated behavior at 24°C (black bar) and 30°C (grey bar). Percentages predicted on the basis of component mechanics (see Discussion) are white bars.

The mechanical properties of the microtubule determine the collision geometry, loading rates, and dictate component failure probabilities. When a particle-laden microtubule encounters a particle-free microtubule, general collision geometries include (Fig. 4.4): a) a "particle-on-top" mode, in which the particle laden shuttle crawls over the particle-free shuttle, should statistically occur 50% of the time resulting in bypass events, b) a "teeter-totter" mode, in which a crossing microtubule is on top and sequentially attaches to one side and then the other of a particle-laden microtubule, and c) a "bridging" mode, in which the crossing microtubule is on top and is attached to the substrate on both sides of the particle. For b) and c), another important geometric factor is the angle between the colliding microtubules. For simplicity, we will only describe the mechanics of encounters between microtubules that are perpendicular to each other.

The length distribution and flexural rigidity (EI) of the microtubules determines whether "teeter-totter" or "bridging" collisions occur. The distance (L) required for a crossing microtubule to reattach to kinesin motors on the far side of an obstacle is given by [3]:

$$L = [\langle x^2 \rangle (3EI)/(kT)]^{1/3} \qquad (1)$$

Where x is the height of the obstacle being crossed and T is temperature. At room temperature, and for x = 25 nm (the microtubule diameter), L is around 2 μm. This means that microtubules shorter than 4 μm will cross in the "teeter-totter" mode, while longer microtubules will cross in the "bridging" mode.

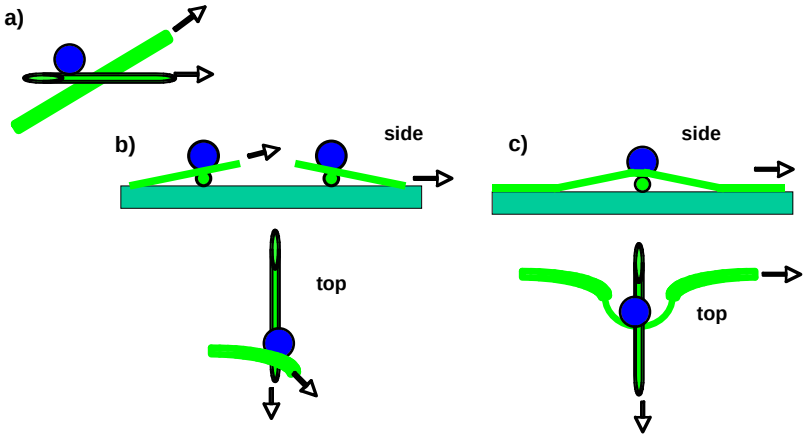

Figure 4.4. Illustrations of major collision geometries: a) the host microtubule (black outline) carries a particle (blue) over an encountered microtubule, b) side (early and late time) and top views of the encountered microtubule crossing and contacting the particle in a "teeter-totter" mode, and c) side and top views of the encountered microtubule bridging the host and its particle cargo.

In "teeter-totter" collisions involving short microtubules, forces and loading rates are dictated by the stresses built up in the crossing microtubule as it is bent by the moving particle it has encountered. In the "worst case" perpendicular collision, the deflected microtubule can be treated as a cantilever spring that is clamped on one side only by kinesin motors, for which:[3]

$$F = (3EI)(y(L))/L^3 \qquad (2)$$

Here, L is the length of the free portion of the microtubule, y(L) is the distance the end of the microtubule is deflected (perpendicular to L), and F is the force the microtubule is exerting on the bound particle. For an experimentally-observed beam-bending encounter (Fig. 4.2b) with L = 1.5 μm, y(L) = 1 μm, and EI = 2.6 x 10^{-23} N-m^2, the calculated force exerted on the particle by the crossing microtubule is 23 pN. Loading rates can be estimated by dividing the force at a given deflection (23 pN) by the time required to achieve the deflection (2.5 s), resulting in a loading rate of 9 pN/s. At this loading rate, the force required to rupture a single streptavidin-biotin bond (37 pN) exceeds the applied force. For this example, the mechanics analysis suggests that the bending microtubule will not supply sufficient force to dislodge the particulate cargo.

In "bridging" collisions involving long microtubules, where the crossing microtubule is clamped on both sides by kinesin motors, the particle experiences the full force applied by the moving shuttle beneath it. As such forces are quite high (up to 1500 pN for a 5 μm shuttle), component failures typically occur before the forces resisting forward motion cause the motors propelling the shuttle to stall out. The first thing that happens is that the clamped microtubule bends in the middle. This bending determines the loading rate. For example, in Fig. 4.2c, the particle moves 0.4 μm at a velocity of 0.4 μm/s after a bridge is formed, resulting in a loading time of one second. The particle is being propelled by a 7

μm microtubule with a net force as high as 2100 pN, resulting in a loading rate of 2100 pN/s. At this loading rate, the force required to rupture the streptavidin-biotin bond is only around 80 pN, which means that at least 26 linkages would be required to keep the particle attached to the shuttle.

Another failure mode associated with a "bridging" collision involves rupture of the microtubule. Microtubule severing will occur when the radius of curvature of the "bridge" is tighter than the 0.6 μm reported to cause failures.[18] The tension (T) built up in the microtubule can be estimated by[19]:

$$T = EI/2R^2 \qquad (3)$$

For the sequence shown in Fig. 4.2f, R at rupture appears to be 0.5-0.6 mm as expected, corresponding to T = 36-52 pN. For the same sequence, the rupture force for the biotin-streptavidin bond is estimated to be 67 pN, indicating that severing should occur prior to particle dislodgement as is observed.

Bypass, bending, particle dislodgement, and microtubule severing events can all occur when a particle-laden microtubule encounters biotin-free microtubules. The final two classes of collisions, microtubule joining and particle transfers, require that free streptavidin on the particle bonds to biotin on the encountered microtubule. For "short" microtubules, the analysis above suggests that joining events, in which no biotin-streptavidin bonds are disrupted, should be preferred relative to transfers, in which bonds to one of the microtubules must be broken. For "long" microtubules, joining events should be rare, as the forces applied are too strong to be sustained by even multiple biotin-streptavidin linkages. However, transfers of the particle to the crossing microtubule should have a high probability relative to particle dislodgement or microtubule severing processes, as the odds for dislodging all linkages to both microtubules simultaneously should be low.

Clearly, collisions between particle-laden colliding microtubules involve complex interactions that are beyond our ability to model in a quantitative fashion. However, with just a few simplifying assumptions, and using the very basic models presented above, we can arrive at distributions for collision events that are in qualitative agreement with experimental observations. All collisions in which the particle-laden microtubule crosses on top are assumed to result in bypass events. For "teeter-totter" collisions involving "short" microtubules, all biotin-free collisions are assumed to result in microtubule bending, while collisions in which streptavidin contacts biotin on the crossing microtubule are assumed to result in joining. For "bridging" collisions with "long" microtubules, all collisions with biotin are assumed to result in particle transfers, while biotin-free collisions are assumed to result in particle dislodgement and microtubule severing (with equal probability for simplicity). With these assumptions, the observed microtubule length distribution (75% are "short"), and the assumption that 50% of all collisions result in the formation of biotin-streptavidin bonds to the encountered microtubule, the predicted distribution for collision events is (Fig. 4.3): Bypass = 50%, Bending = 19%, Joining = 19%, Transfers = 6%, Knock-Off = 3%, and Severing = 3%. This distribution compares well with the distribution observed in experiments at 25^{o}C: Bypass = 45%, Bending = 20%, Joining = 18%, Transfers = 10%, Knock-Off = 5%, Severing = 1%. A more detailed analysis of the composition of colliding components

and the exact geometries of each collision would be required to provide quantitative predictions that could be directly compared with our experimental results. However, the analysis does suggest that the distribution of collision events should be sensitive to component attributes including the length of the microtubules, the loading rate dependent rupture force of linker groups, and the concentrations and accessibility of linker components (e.g. biotin and streptavidin) on the microtubules and particles, respectively.

4.6 Conclusions

The use of motor proteins and microtubules to transport and assemble objects in microfluidic systems requires controlling interactions between microtubule shuttles, the cargo, and other objects in the system such as channel walls. For transport in microchannels, shuttle motion must not be impeded by components sticking to each other or to channel walls. Conversely, for cargo harvesting and delivery, the cargo must interact with channel walls to allow hand-offs to occur without impeding shuttle motion. The development of active transport systems based on motor proteins requires understanding the physics of shuttle collisions leading to design rules for component optimization. The experiments reported here have allowed us to identify some of these design rules. For active transport of relatively large particles, unimpeded transport will occur when shuttle collisions are strongly biased to favor bypass and bending events relative to other possible outcomes. An analysis based on the nanomechanics of our interacting components indicates that this can be achieved by utilizing shuttles that are shorter than 4 μm long (minimizing severing, knock-off, and transfer events) and by using minimal functional groups concentrations to affix cargo to microtubules (minimizing the probability of joining events and shuttle agglomeration). (The appropriate design rules for transporting sub-micron particles are addressed elsewhere[20]). For cargo transfers, optimized loading and unloading zones may ultimately involve the use of interfaces whose interactions can be switched using "on-chip" stimuli.[21] The results reported here suggest that another design feature for cargo-handling stations may involve controlling the compliance of cargo handling zones. For strain-rate-dependent linkages such as the biotin-streptavidin bond, our analysis suggests that compliant materials, such as the "long" microtubule bridges observed here, will be more effective at harvesting particles than more rigid objects such as channel walls. This is because more compliant objects subject colliding objects to lower loading rates, which can lower the force required to disrupt strain rate-dependent linkages by over an order of magnitude. With optimized linkers, it may be possible to design cargo loading and unloading zones by using "hard" and "soft" materials for these respective zones. Both switching and compliance strategies are being designed into our next generation of active transport systems.

4.7 References

(1) Alberts, B., et al., *Essential Cell Biology*; Garland Publishing, Inc.; New York, 1998

(2) (a) Montemagno, C. D. *J. Nanopart. Res.* **2001**, *3*, 1-3. (b) Soong, R. K.; Bachand, G. D.; Neves, H. P.; Olkhovets, A. G.; Craighead, H. G.; Montemango, C. D. *Science* **2000**, *290*, 1555-1558. (c) Bachand, G. D.; Soong, R. K.; Nevas, H. P.; Olkhovets, A.; Craighead, H. G.; Montemango, C. D. *Nano Lett.* **2001**, *1*, 42-44. (d) Liu, H.; Schmidt, J. J.; Bachand, G. D.; Rizk, S. S.; Looger, L. L.; Hellinga, H. M.;

Montemango, C. D. *Nature Mater.* **2002**, *1*, 173-177. (e) Bunk, R.; Klinth, J.; Rosengren, J.; Nicholls, I.; Tågerund, S.; Omling, P.; Månsson, A.; Montelius, L. *Microelec. Eng.* **2003**, *67-67*, 899-904.

(3) Howard, J. Mechanics of Motor Proteins and the Cytoskeleton; Sinauer Associates, Inc.; New York, 2001

(4) Asbury, C. L.; Fehr, A. N.; Block, S. M. *Science* **2003**, *302*, 2130-2134.

(5) Straight, A. F., Field, C. M. *Current Biol*., **2000**, *10*, R760.

(6) (a) Hess, H.; Matzke, C. M.; Doot, R. K.; Clemmens, J.; Bachand, G. D.; Bunker, B. C.; Vogel, V. *Nano Lett.* **2003**, *3*, 1651-1655. (b) Clemmens, J.; Hess, H.; Lipscomb, R.; Hanein, Y.; Bohringer, K. F.; Matzke, C. M.; Bachand, G. D.; Bunker, B. C.; Vogel, V. *Langmuir* **2003**, *19*, 10967-10974.

(7) (a) Howard, J., Hudspeth, A. J., Vale, R. D. *Nature* **1989**, *342*, 154. (b) Hiratsuka, Y., Tada, T., Oiwa, K.; Kanayama, T., Uyeda, T. Q. P. *Biophys. J.* **2001**, *81*, 1555. (c) Howard, J.; Hunt, A.; Baek, S. *Method. Cell. Bio.* **1993**, *93*, 137-147.

(8) Bachand, G. D.; Rivera, S. B.; Boal, A. K.; Gaudioso, J.; Liu, J.; Bunker, B. C. *Nano Lett.* **2004,** *4*, 817.

(9) For recent examples, see: (a) Caswell, K. K.; Wilson, J. N.; Bunz, U. H. F.; Murphy, C. J. *J. Am. Chem. Soc.* **2003**, *125*, 13914-13915. (b) Wang, J.; Li, J.; Baca, A. J.; Hu, J.; Zhou, F.; Yan, W.; Pang, D.-W. *Anal. Chem.* **2003**, *75*, 3941-3945. (c) Star, A.; Gabriel, J.-C. P.; Bradley, K.; Gruner, G. *Nano Lett.* **2003**, *3*, 459-463. (d) Valimaa, L.; Pettersson, K.; Vehniainen, M.; Karp, M.; Lovgren, T. *Bioconjugate Chem.* **2003**, *14*, 103-111. (e) Zhou, D. J.; Bruckbauer, A.; Ying, L. M.; Abell, C.; Klenerman, D. *Nano Lett.* **2003**, *3*, 1517-1520. (f) Cobbe, S.; Connolly, S.; Nagle, L.; Eritja, R.; Fitzmaurice, D.; Ryan, D. *J. Phys. Chem. B.*, **2003**, *107*, 470-477.

(10) Böhm, K. J.; Stracke, R.; Mühlig, P.; Unger, E. *Nanotechnology* **2001**, *12*, 238-244.

(11) Diez, A.; Reuther, C.; Dinu, C.; Seidel, R.; Mertig, M.; Pompe, W.; Howard, J. *Nano Lett.* **2003**, *3*, 1251-1254.

(12) Reznik, G. O.; Vajda, S.; Cantor, C. R.; Sano, T. *Bioconjugate Chem.* **2001**, *12*, 1000-1004.

(13) Merkel, R.; Nassoy, P.; Leung, A.; Ritchie, K.; Evans, E. *Nature*, **1999**, *307*, 50-53. (a) Yuan, C.; Chen, A.; Kold, P.; Moy, V. T. *Biochemistry* **2000**, *39*, 10219-10223. (b) Lo, Y-S.; Zhu, Y.-J.; Beebe, T. P. Jr. *Langmuir*, **2001**, *17*, 3741-3748.

(14) Hess, H.; Howard, J.; Vogel, V. *Nano Lett.* **2002**, *2*, 1113-1115.

(15) Lo, Y.-S.; Simmons, J.; Beebe, T. P. Jr *J. Phys. Chem. B* **2002**, *106*, 9847-9852.

(16) Kawaguchi, K.; Ishiwata, S. *Biochem. Biophys. Res. Comm.* **2000**, *272*, 895-899.

(17) Coy, D. L.; Wagenbach, M.; Howard, J. *J. Biol. Chem.* **1999**, *274*, 3667.

(18) Waterman-Storer, C. M.; Salmon, E. D. *J. Cell Biol*. **1997**, *139*, 417.

(19) Arai, Y., et al. *Nature* **1999**, *399*, 446.

5.0 Application of Selectively Functionalized Microtubules for the Assembly of Polar –Oriented Synthetic Organized Microtubule Organizing Centers

Erik D. Spoerke, George D. Bachand, Jun Liu, Darryl Sasaki, and Bruce C. Bunker

5.1 Introduction

Microtubules (MTs) are polar cytoskeletal fibers whose function and performance in living systems is commonly dependent on their positioning around microtubule organizing centers (MTOCs), such as centrosomes in animal cells. Polymerized from monomeric α and β tubulin, these organized MT structures influence a diverse array of cellular functions, ranging from positioning chromosomes within a cell nucleus during cell division to serving as tracks for motor protein-based intracellular cargo transport. The precise organization of the MTs as they perform these diverse functions is carefully regulated and directed by a complex collection of proteins that serve to nucleate, orient, and stabilize the MTs according to their appropriate function.

Previous reports describe attempts to artificially recreate or mimic these organized MT constructs on silica or magnetic beads[1,2]. Another elegant engineered approach was demonstrated by Nedelec, *et al.*[3], where modified kinesin motor protein "constructs" were used to organize elegant, densely packed MT asters. Taking a more direct biological approach, others have demonstrated the *in vitro* reconstitution of MTs around isolated centrosomes[4-6].

Of these cases, only the reconstitution of the centrosomes and the use of the motor constructs have the ability to direct the polarity of the MTs in their organization, a characteristic critical to the function of the MTs. The growth of MTs around the centrosomes is nucleated and directed by γ-tubulin protein complexes which bind to the "minus" end of the microtubules, imparting polarity to the tubes[7,8]. This system, however, lacks the ability to create "inversely" polar tubes, such that the "plus" end of the MTs would be directed centrally. On the other hand, the polarity of the MTs in the asters created by motor constructs is derived from the inherent polar interaction with the MTs. Because the kinesins inherently move along the MTs from "minus" to "plus," the motor-directed organization of these tubes is necessarily polar. Using the specific kinesin constructs described by Nedelec *et al.*,[3] however, inverted polar structures will also be inaccessible because of the specific protein-based directionality of the assembly.

We describe here a more direct method for assembly of polar-oriented synthetic MT organizing centers (POSMOCs). We take advantage of the polar character of MT polymerization to selectively functionalize controlled regions of growing MTs. These functional handles on the MTs, then, can be used to direct their polar organization around a synthetic organizing center. We specifically describe the assembly of these POSMOCs, demonstrating centrally-directed "plus" and "minus" end MT configurations, as well as the creation of "bridged" configurations.

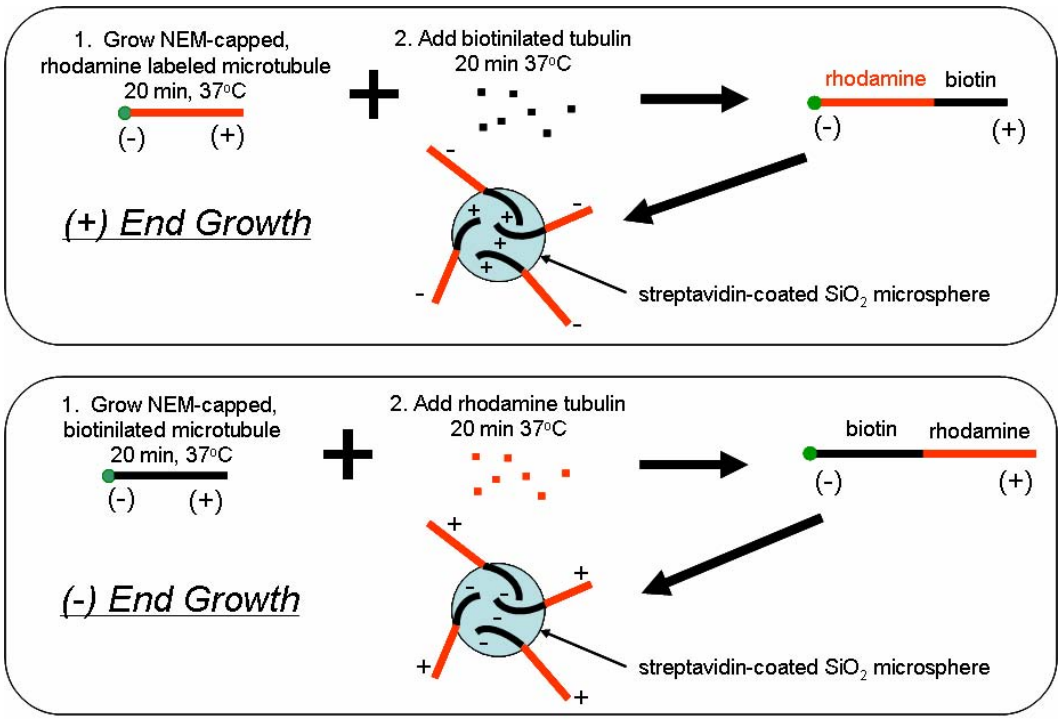

Figure 5.1: Schematic illustration of multistage MT polymerization and assembly into "plus" end (above) and "minus" end (below) POSMOCs.

5.2 Methods and Materials

All tubulin was obtained from Cytoskeleton, Inc (Denver, CO). Chemical reagents were provided by Sigma (St. Louis, MO). Silica microspheres were purchased from Bangs Laboratories (Fishers, IN). Streptavidin-labeled quantum dots were obtained from Quantum Dot Corporation (Hayward, CA).

The methods for assembly of POSMOCs are illustrated schematically in Fig. 5.1. MTs were capped during growth to prevent polymerization in the "minus" direction using N-ethylmaleimide (NEM).[9,10] Monomeric, unlabelled tubulin was dissolved at 5 mg/mL in BRB80 (80 mM piperazine bis(ethanesulfonic acid), 1 mM $MgCl_2$, 1 mM ethylene glycol bis(b-aminoethyl ether-N,N,N,',N'-tetraacetic acid (EGTA), pH 6.9). This tubulin was first reacted with 1 mM N-ethyl-maleimide (NEM), 0.1 mM guanosine 5'-triphosphate (GTP) in water for 10 min at 0°C before quenching with 8mM β-mercaptoethanol (BME) for 10 min at 0°C. Excess BME, GTP, and NEM were removed using a Biorad P6 spin column.

Polymerization of "plus" end functionalized MTs was achieved by combining 2 μL of 5 mg/mL NEM-capped tubulin in BRB80P (BRB80 + 10% glycerol + 1 mM GTP) with 2 μL rhodamine-labeled tubulin in BRB80P. After 20 minutes, 10 μL biotinylated tubulin, diluted 10X in BRB80P was added directly to the polymerizing tubes. Following

a 20 minute polymerization of this mixture at 37°C, the polymerized MTs were stabilized by the addition of 200 μL of BRB80T. MTs were collected by centrifugation at 20,000 x g and resuspended in 10 μL of BRB80TAF (BRB80T in 20mM dextrose + 0.02mg/mL glucose oxidase, 8 μg/mL catalase, and 0.5% β-mercaptoethanol).

Polymerization of "minus" end functionalized MTs was achieved using identical methods, but using biotinylated tubulin in place of rhodamine-labeled tubulin and vice-versa. Similarly, bipolar-functionalized microtubules were produced just as the "plus" end functionalized MTs were created, but no NEM capping was used.

Functionalization of silica microspheres was achieved by first washing 100 μL of 2.34 μm silica microspheres 3x with BRB80, then 2x with chloroform, collecting beads by centrifugation in a Galaxy benchtop centrifuge. Beads were then treated for 20 min at room temperature in a 10 mM solution of 3-Aminopropyltriethoxysilane (APTES) in chloroform. Following silanization, beads were rinsed 3x with chloroform and then dried and annealed at 60°C for 1 hour. These amine-functionalized beads were then suspended with a 10 mM Biotin-Nitrophenyl ester in tetrahydrofuran (THF) at 55°C for 1 hour. Following 3 rinses with THF and 2 rinses with phosphate buffered saline (pH 7.4), beads were incubated with Oregon Green-labeled streptavidin, diluted 10X in 1 mL of PBS, for at least 10 minutes before use and stored at 4°C.

The POSMOCs were assembled by first rinsing 1 μL of streptavidin-functionalized microspheres 2X in BRB80 to exchange buffers. Beads were then incubated for 10 minutes in BRB80 containing 0.5 mg/mL casein. Beads were then rinsed with BRB80 and resuspended in 10 μL of polar MTs in BRB80TAF as synthesized above. This suspension was allowed to incubate at room temperature for a minimum of 10 minutes before flowing into a cover slip flow cell comprising two glass cover slips separated by two pieces of double-sided clear tape, spaced approximate 5 mm apart. After approximately 30 minutes, streptavidin-labeled quantum dots, diluted 1000x in BRB80TAF, were introduced to the flow cell and allowed to incubate 2 minutes before rinsing with BRB80TAF.

To test the polarity of the functionalized MTs, they were examined using an inverted motility assay[11,12]. Twenty microliters of BRB80 containing 0.5 mg/mL of casein was introduced to a blank cover slip flow cell and allowed to incubate at room temperature for 5 minutes. *Drosophila melanogaster* dimeric kinesin proteins, expressed and purified from *Escherichia coli*[13], were flowed into the cell and allowed to incubate another 5

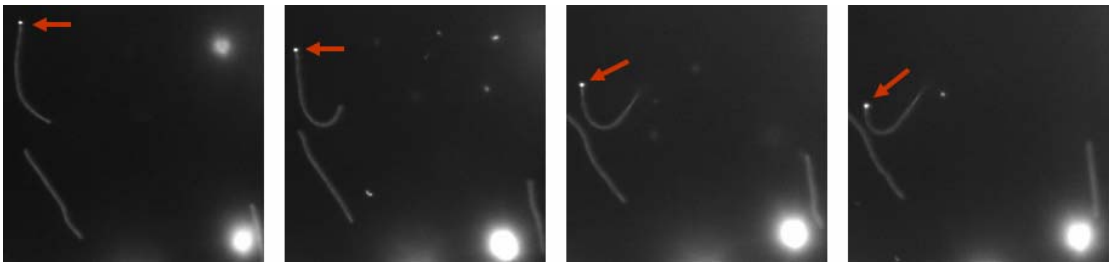

Figure 5.2: Fluorescent microscope image series showing polar-functionalized MT movement over an array of kinesin motor proteins. The MT is moving with the "minus" end in front, and is dragging a streptavidin quantum dot (indicated by arrows), bound to the biotinylated "plus" end of the MT.

minutes. A suspension of polar MTs and streptavidin-labeled microspheres (dragon green fluorescent, 0.5 μm) in motility buffer (BRB80TAF containing 100 μM adenosine triphosphate (ATP)) was then introduced to the cell and microtubule motility was observed by fluorescence microscopy.

5.3 Results and Discussion

The multistage polymerization was found to be an effective method for the synthesis of polar-functionalized MTs. Fig. 5.2 demonstrates an example of this success with a series of images showing the movement of a "plus" end functionalized MT over an array of kinesin motors. The images show a streptavidin-coated quantum dot (indicated by arrows) bound to the biotinylated "plus" end of the MT. These kinesin motor proteins only move in the "plus" direction along MTs, which means that in the inverted motility

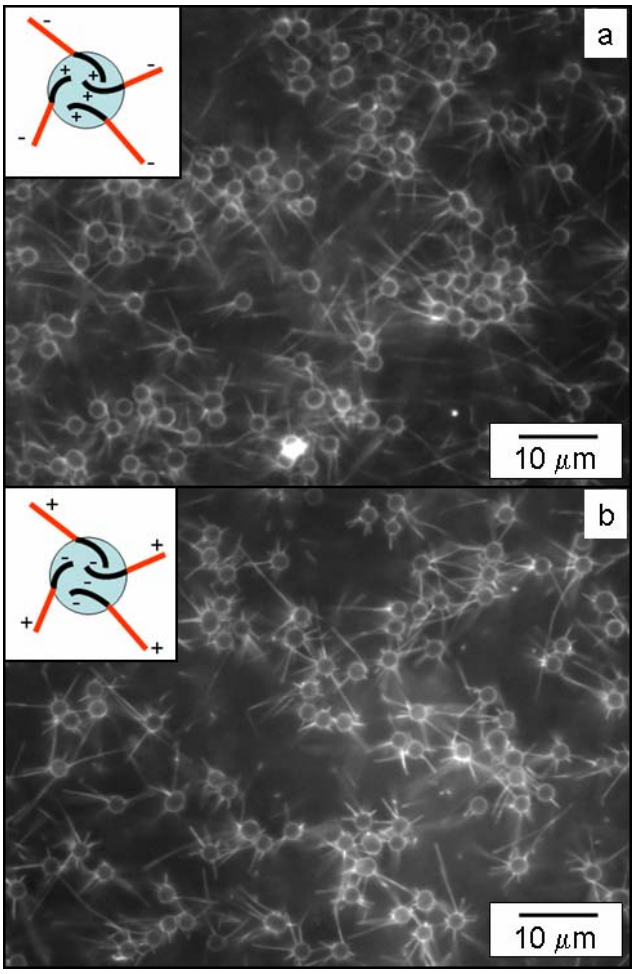

Figure 5.3: (a) POSMOCs with "plus" end directed towards microsphere (b) POSMOCs with "minus" end directed towards microsphere. In each case, MTs can be seen extending radially from the functionalized microsphere organizing centers. Each microsphere is approximately 2.3 μm in diameter.

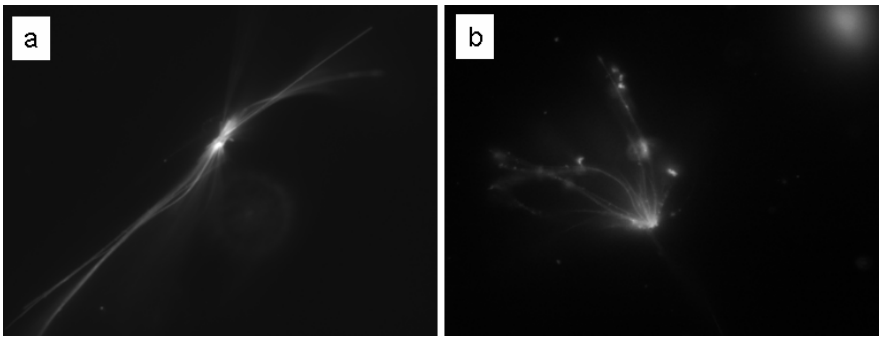

Figure 5.4: Fluorescent images showing examples of microtubule asters formed from "minus" end functionalized MTs. Asters are formed when streptavidin-coated quantum dots bind the biotinylated ends of the polar functionalized MTs centrally.

assay, the MTs should move with the "plus" end toward the rear of the moving MT. The images in Fig. 5.2 clearly show that the quantum dot is bound only at one end of the MT, illustrating the functionally segmented nature of the polar tubes. Furthermore this functional end is at the rear ("plus" end) of the MT. These results show that the integration of a multistage polymerization process and the chemical modifier NEM makes it possible to create MTs with functional components, spatially resolved with respect to the MTs' polarity.

The assembly of these polar structures into POSMOCs is revealed in Fig. 5.3. First, the bright fluorescence emitted from the microspheres themselves comes from the Oregon green-labeled streptavidin, confirming the presence of streptavidin binding sites on the microspheres. Fig. 5.3a, then, shows MTs formed around microspheres, with the biotin-functionalized "plus" ends of the MTs directed inward, bound to the streptavidin-labeled microspheres. By contrast, Fig. 5.3b shows MTs organized with the "minus" ends of the MTs directed toward their organizing centers. In both cases the non-biotinylated regions of the MTs extend radially from the organizing centers, similar to the MT organization seen around centrosomes. In cases where either non-biotinylated MTs were used or the silica spheres were not functionalized, MTs did not form these synthetic asters. Interestingly, when quantum dots were substituted for the functionalized microspheres, local concentrations of functionalized quantum dots effectively condensed and bound the functional ends of the polar MTs, producing a different form of MT aster. Examples of these structures are illustrated in Figs. 5.4a and 5.4b, made from "minus" end functionalized MTs. The relatively high concentration of quantum dots holding the MTs together gives rise to the brightly fluorescing organizing centers in these structures. These results are clear evidence of how the spatially-controlled chemical function within the polymerized MTs can be used to direct their assembly into complex structures, reminiscent on biological organizing centers.

In the cases where no NEM capping was applied, the MTs were formed with biotinylated functionality on both ends of the MTs. Such structures demonstrated the ability to bridge two organizing centers, as shown in Fig. 5.5. The image in Fig. 5.5a shows the fluorescence from both the rhodamine-labeled tubulin and quantum dots that have been attached to the biotinylated segments of these MTs. This image shows that the MT clearly extends between the two streptavidin-labeled microspheres. The image in Fig. 5.5b shows only the fluorescence emitted from the quantum dots. These quantum dots,

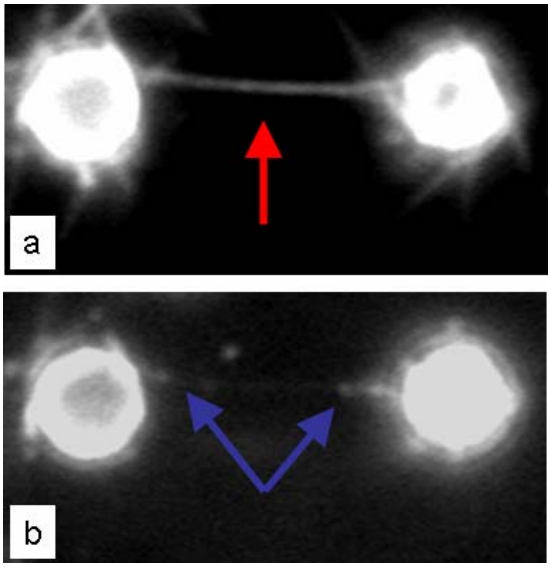

Figure 5.5: Fluorescent images showing a MT bridging two microsphere organizing centers. (a) Fluorescence (Ex: ~550 nm) from rhodamine-labeled and quantum dot-labeled regions of the MTs shows the MTs extending between both microspheres. (b) Fluorescence (Ex: ~365nm) from streptavidin-labeled quantum dots only shows that the quantum dots are bound only to the biotinylated ends of the MT bridge, demonstrating the chemically-functional segmenting of the bridging MT.

bound to the biotinylated regions of the MT, are localized at the ends of the MT where the MT is binding to the streptavidin-coated microsphere. These images suggest that the binding of the MT to the microsphere is mediated by the linkage between the biotinylated end segments of the MT and the streptavidin-functionalized surfaces of the microspheres. When the NEM is not used, there is significant polymerization on both ends of the MT. These observations are consistent with previous work by Bachand *et al.*[11], who used a similar, multistage approach to MT polymerization to create quantum dot-MT nanocomposites. The current work demonstrates a wider applicability of this approach, illustrating how the multifunctional structure of these MTs may be used to manipulate their organization into designed architectures.

This result not only demonstrates the feasibility of applying these processes to creating microtubule bridges, but also stresses the relative importance of using NEM capping to create consistently polarized MTs. Previous work has described the potential polarity of MTs grown from seeded microbeads, based on the premise that faster polymerization in the "plus" direction would lead to longer MTs being polarized[2]. The current work, however, has demonstrated that for the selective functionalization methods described herein, preferential growth in the "plus" direction is not sufficient to insure that the secondary growth (either biotinylated ("plus" end functionalized) or rhodamine-labeled ("minus" end functionalized)) will be restricted to the "plus" end. Rather, the use of a capping agent, such as NEM is necessary to facilitate this control.

5.4 Conclusions

This approach to POSMOC assembly represents a simple, versatile methodology for the manipulation of microtubule structures. Through controlled, multistage polymerization, it is possible to create spatially-resolved chemistry within microtubules. This defined chemical character may then be utilized in directing the organization of the microtubules to create complex synthetic assembles with polar organization of the microtubules. Future work introducing motor proteins to these constructs holds great promise for active assembly of complex nanoscale multimaterials. This biologically-mediated approach to materials assembly has tremendous potential to improve the way nanomaterials will be integrated into functional technologies.

5.5 References

(1) Faivre-Moskalenko, C.; Dogterom, M. *Proc. Natl. Acad. Sci. USA,* **2002**, *99*, 16788.
(2) Holy, T.; Dogterom, M.; Yurke, B.; Leibler, S. *Proc. Natl. Acad. Sci. USA*, **1997**, *94*, 6228.
(3) Nedelec, F.; Surrey, T.; Maggs, A.; Leibler, S. *Nature*, **1997**, *389*, 305.
(4) Mitchison, T.; Kirschner, M. *Nature*, **1984**, *312*, 232.
(5) Schnackenberg, B.; Khodjakov, A.; Rieder, C.; Palazzo, R. *Proc. Nat. Acad. Sci. USA*, **1998**, *95*, 9295.
(6) Stearns, T.; Kirschner, M. *Cell*, **1994**, *76*, 623.
(7) Inclan, Y.; Nogales, E. *J. Cell Sci.* **2000**, *114*, 413.
(8) Leguy, R.; Melki, R.; Pantaloni, D.; Carlier, M.-F. *J. Biol. Chem.* **2000**, *275*, 21975.
(9) Hyman, A.; Dreschel, D.; Kellogg, D.; Salser, S.; Sawin, K.; Steffen, P.; Wordeman, L.; Mitchison, T. *Methods Enzymol.* **1991**, *196*, 478.
(10) Phelps, K.; Walker, R. *Biochemistry*, **2000**, *39*, 3877.
(11) Bachand, G. D.; Rivera, S. B.; Boal, A. K.; Gaudioso, J.; Liu, J.; Bunker, B. C. *Nano Lett.* **2004**, *4*, 817.
(12) Howard, J.; Hunt, A.; Baek, S. *Methods Cell Biol.* **1993**, *39*, 137.
(13) Coy, D. L.; Wagenbach, M.; Howard, J. *J. Biol. Chem.* **1999**, *274*, 3667.

6.0 Engineering micromachined piconewton force sensors for biophysics investigations

Steven J. Koch, Gayle E. Thayer, Alex D. Corwin, and Maarten P. de Boer

6.1 Abstract

We describe a polysilicon surface-micromachined force sensor that is able to measure forces as small a few pN in both air and water. The simple device consists of compliant springs with force constants as low as 0.3 mN/m and Moiré patterns for nanometer-scale optical displacement measurement. First, we measured the force field produced by an electromagnet on individual 2.8 μm magnetic beads glued to the force sensor. Forces matched predictions from finite element magnetic modeling and provided a calibration for future biophysical applications of the magnet. By repeating with several different beads, we measured a 9% standard deviation in saturation magnetization. We also demonstrated that the force sensor was fully functional when immersed in aqueous buffer and when performing the kinesin inverted motility assay on the sensor surfaces. These results show the force sensors can be useful for calibrating magnetic forces on magnetic beads and also for direct measurement of biophysical forces on-chip.

6.2 Introduction

Functionalized magnetic microspheres are useful for a variety of intra-cellular and molecular biophysics applications[1-7], but their utility depends on the ability to apply well-controlled and calibrated forces. Popular calibration methods have relied on inference of force from Stokes drag[3,4,8] and Brownian dynamics[1], while other methods have used calibrated microneedles[6,9], gravity[10] or known properties of polymers[11]. While very useful, these methods have drawbacks in some cases. In Stokes drag calibration, the particle radius and solvent viscosity must be known accurately, and also the magnetic particle may travel a large distance compared with the particle diameter, leading to complications when the field gradient is large. When using Brownian dynamics, the length of the tether must be measured or deduced, and the temperature must be well controlled. To address these complications, we have designed, fabricated and tested a compliant surface-micromachined spring with which the lateral force field of an electromagnet on a single magnetic microparticle can be calibrated. This provides a simple force calibration method that does not depend on particle shape, polymer tethers of known length, or solvent conditions. Furthermore, the spring is sensitive enough to allow characterization of single bead, and therefore, bead to bead variation.

The principle of our device is similar to previous reports using long glass cantilevers[6,9], but with some important distinctions. While a long glass fiber is ideal for placing a microsphere into a very small gap, each fiber must be individually calibrated and may not have an easily controlled spring constant. In the device we describe here, the spring constant can be chosen by design, and can be accurately verified by on-chip calibration. Furthermore, the device can operate both in air and water, leading to future possibilities of directly measuring biophysical forces on-chip with multiple adjustable sensors.

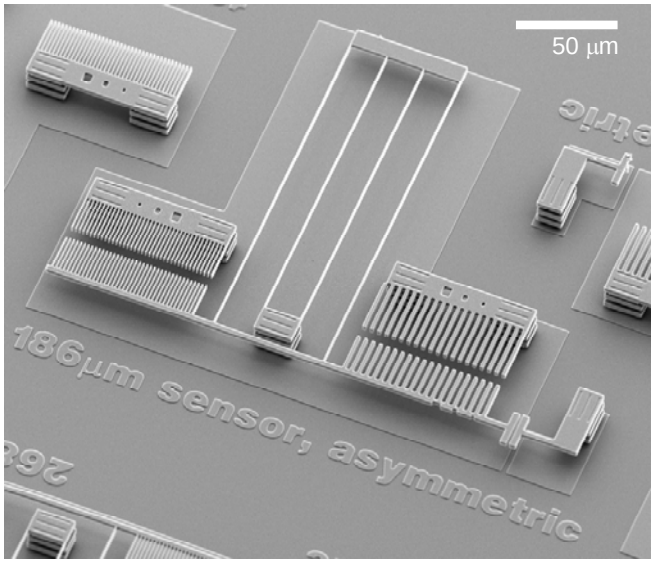

(a)

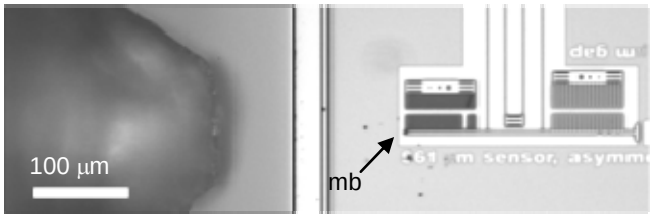

(b)

Figure 6.2. (a) SEM image of a 186 μm force transducer (30 pN / nm), scale bar 50 micron. Stiffer force sensor is shown for ease of display, while a longer, 581 force sensor (1 pN / nm) is used for data in this report. (b) 10x picture of device with single bead positioned next to the electromagnet, scale bar 100 micron. Position of single magnetic bead indicated by arrow.

6.3 Design and fabrication of surface-micromachined force sensors

As seen in Fig. 6.1(a), the device consists of a folded-beam suspension attached to a Moiré grating. It is fabricated by surface micromachining methods[12], and the structural

material is polycrystalline silicon (polysilicon). The spring constant of the grating can be determined from:

$$k = 2E(w - \Delta w)^3 t\left(L_o^3 + L_i^3\right)^{-1} \qquad (1)$$

where E =164 GPa[13] is Young's modulus, w = 1 μm is the nominal linewidth, Δw = 0.23 μm (as measured by high-resolution SEM) is the decrease in the nominal linewidth due to processing, t = 2.25 μm is the spring thickness and L_o and L_i are the respective lengths of the outer and inner spring beams. For these designs, L_o-L_i = 19 μm, and L_o values were 186, 268, 388, 561 and 823 μm, for nominal spring constant values of 34, 11, 3, 1 and 0.3 mN/m.

The displacement sensor is comprised of an object grating attached to the end of the spring and a reference grating attached to the substrate. The grating pitch is accurate to ± 20 nm. To make a displacement measurement, we compare the relative phase of the two gratings. Using a 50x objective, by applying sub-pixel interpolation and by virtue of averaging over the many pixels of the periodic grating, we can detect phase to one part in one thousand. Given the grating pitch of 2.5 μm, this translates to 2.5 nm in-plane measurement resolution. Force resolution is then the product of the displacement measurement and the spring constant.

During fabrication, a 12-μm thick silicon oxide material is deposited on the substrate while the polysilicon post is built by repeated deposition, lithography and etching steps. The polysilicon spring layer is then formed. The oxide material is selectively removed in an HF:HCl acid and transferred to water. The most challenging step in the fabrication is the drying of the compliant structures. Critical point drying (CPD) with supercritical carbon dioxide is used as the working fluid[14] to render structures freestanding. Although this process in principle avoids capillary-induced adhesion, we can expect that either (i) flow or (ii) trace liquids can exert some force on these very compliant structures. Generally, structures with $L_{out} \leq 561$ μm or less yielded well, while L_{out} = 823 μm did not reproducibly survive the CPD process. It should be noted that for these lengths, gravity is negligible and the sensor is at the same height as the support post.

6.4 Magnetic force measurements

Using two micromanipulators and pulled-glass fibers, we affixed with vacuum grease individual beads (Dynal M270 streptavidin, product #653.05, lot# F72000) to a desired location on the MEMS force sensor with approximately 5 μm precision. Fig. 6.1b shows a single bead affixed to a sensor and positioned about 200 μm away from the magnet face. The process required about 10 minutes per bead and was efficient enough to allow us to individually characterize 9 beads and thus obtain a distribution of saturation moments. To minimize uncertainty due to possible Δw variations, force sensors fabricated in close proximity (~300 μm apart) was used for these measurements. That is, beads were applied, characterized and then removed before a new bead was placed on three adjacent sensors. Fig. 6.2 shows force versus magnet current for 9 different beads at an axial distance of 200 μm from the magnet pole piece. We assumed the saturated bead moment to be proportional to bead displacement at a maximum applied current

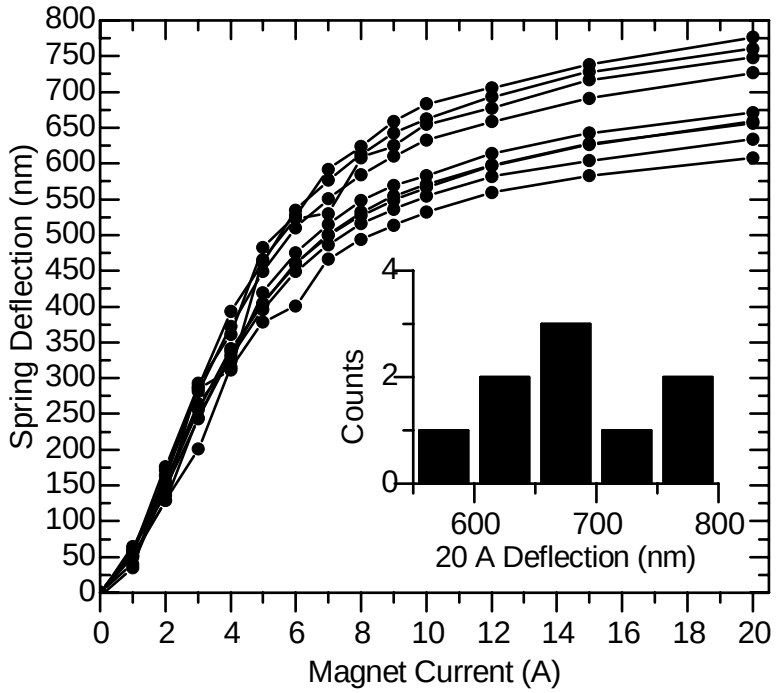

Figure 6.2. Measured spring deflection versus magnet current for [nine] different beads on three different sensors. Each trace represents an individual non-averaged sweep with current increasing from 0 to 20 amps. Magnet degaussed prior to each sweep. (Inset) Histogram of spring deflection at 20 amps, bin size 50 nm. Each measurement represents an average displacement from nine successive image frames (to reduce noise from stray air currents).

(20A, field = 560 mT), and constructed the histogram shown in the inset by averaging 9 consecutive measurements after stepping current from 0 to 20 A. For the 9 beads we measured a standard deviation of +/- 9%. Previous researchers had measured a 72% and 41% standard deviation for a similar magnetic microsphere (Dynal M280)[8,15]. Our much lower standard deviation could reflect improvements in the commercial preparation, or could also reflect uncertainties that arise from the two previous technique's sensitivity to other factors besides force—namely bead shape, radius, and viscous coefficient in the former, and orientation and separation of bead from giant magnetoresitive sensor in the latter. It should also be noted that a potentially high throughput technique based on balance between magnetic gradient, gravitational, and Stokes forces has also been reported[16]; the particles characterized, however, are not directly comparable, and further, the technique again relies on many further parameters besides a simple spring constant. We believe that use of a mechanical spring simplifies the bead to bead variation measurement and improves precisions as demonstrated by a less than 1% variation measured for a control bead that remained affixed to a fourth sensor throughout all experiments (data not shown).

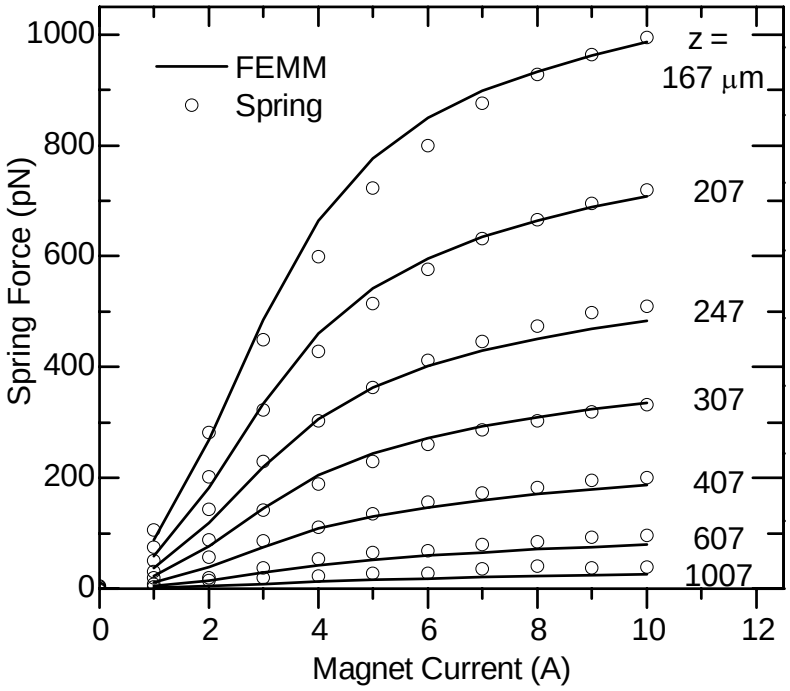

Figure 6.3. Measured (open circles) and calculated (lines) force versus applied magnet current for seven different axial displacements of a single bead (from top: 167, 207, 247, 307, 407, 607, 1007 μm). Calculated values use the best fit value for magnetite weight / weight content of 59% as described in text.

For a magnet current of 20A and pole-to-bead distance of 200 μm the field is approximately 560 mT, and thus, anisotropy should not be a cause of bead to bead variation. Therefore, the most likely cause of polydispersity is magnetite content, which is a combination of magnetite volume fraction and bead volume. A 3% standard deviation in particle diameter (the upper limit of manufacturer's specifications) could account for the variation we see in saturated bead moment. However, our current method is unable to distinguish between variations due to particle size or magnetite volume fraction.

We also used the micro-spring to calibrate the force field on a single bead for various currents and axial displacements from the pole, as shown in Fig. 6.3. For a given distance, the data represent a single current sweep (0 to 10 A), and the same bead and sensor were used for all data. Prior to each current sweep, the magnet was degaussed with a decaying 100 Hz current. As expected, due to remnants in the iron core, the return sweeps (not shown) showed significant hysteresis.

Using axisymmetric finite element magnetic modeling (FEMM)[17] we deduced the magnetite content of the bead by fitting the force curves to the FEMM predictions (assuming a 2.8 μm diameter and an initial susceptibility of 1 and saturation magnetization of 208,000 A/m for the magnetite nanocrystals). The magnet was modeled with pure copper wire and a perfectly conical pure iron core with an included angle of 64 degrees and a blunt tip diameter of 2.75 mils. Accuracy of the FEMM predictions of the magnetic field and gradient were roughly confirmed using a 3-axis hall probe with a field sensitive volume of approximately 250 microns per axis (SENTRON model 3M12-2-2-2T). The solid lines in Fig. 6.3 show the FEMM for the best fit magnetite volume fraction

of 59 %. This value is significantly higher than the manufacturer's stated value of 20%, but closer to the value of 32% we obtained with SQUID. The shapes of the FEMM curves do not depend on the assumed magnetite content, and the overall trend agrees very well with the MEMS data. The agreement across a wide current range and axial displacement lends confidence to the magnet force field calibration, and validates the micro-spring as a robust method for calibrating a magnet/microsphere system for use in biophysical applications.

Another feature of the spring force transducer is its relative insensitivity to environmental conditions such as temperature and solvent. We rendered the surface hydrophilic with an ozone treatment, and then using a simple flow cell, we hydrated the device and demonstrated retention of full functionality. The hydrated force measurements were unchanged and noise was significantly damped compared with operation in air. We found that the major source of noise was stray air currents. Because results in buffer were the same as in air, it was not necessary to hydrate the device to characterize our magnet. However, we envision a class of experiments where it will be useful to obtain in-situ force measurements using the mechanical spring. To demonstrate the viability of this line of experiments, we found that the standard kinesin/microtubule inverted motility assay was functional on the MEMS device (we saw a similar velocity as is seen at room temperature on glass). The geometry of the current device design, however, was not suitable for measuring forces from the molecular motors. Our next goal is to optimize the sensor geometry to guide molecular motors and to measure, for example, the stall force of a MT shuttle driven by multiple motors, without need for attaching microspheres or other handles. The stall force of a MT driven by a single kinesin molecule (~ 7 pN)[18] is well within the force sensor resolution, and the stall force for a MT driven by a collection of kinesin motors is likely higher but unknown. Measuring the stall force versus kinesin surface density will be an important measurement relevant to microfluidic devices utilizing the kinesin/MT transport system.

In addition to this example, there are other possible advantages to on-chip real-time force sensing. As seen in Fig. 6.3 the force for this magnet can vary by as much as a factor of two across a distance of 40 microns, so one would need to accurately know the position of the magnet relative to the bead in order to know the force from magnet current alone (one would also have to know the hysteretic properties of the magnet). Real time force sensing would obviate the need to know the precise location of the bead and magnet properties.

6.5 Conclusions

We have shown that a simple micromachined force sensor can be used to characterize individual micron-scale magnetic particles and also to map the magnetic force field of an electromagnet. In the current implementation, the spring constant is determined via the fabricated line width and design parameters, but future designs will incorporate on-chip self calibration. This will enable us to better address the issue of whether 58% is truly the magnetite content. Self-calibration combined with the insensitivity to temperature and buffer conditions make the force sensor an attractive alternative to standard calibration techniques. We anticipate using the device for characterization of other commercial and custom microsphere preparations and other electromagnet designs. Furthermore, we anticipate incorporating the force sensor into future MEMS designs which will be used to

measure biophysical forces in real time for a variety of biomolecular and sub-cellular processes.

6.6 Acknowledgement

The authors gratefully acknowledge the sample fabrication by the Microelectronics Development Laboratory staff and management at Sandia National Laboratories. We are grateful for SQUID measurements performed by Gene Venturini, SEM by Bonnie Mckenzie, FEM mechanical analysis of sensor design by Frank DelRio, and for access to the micromanipulator instrumentation in the Materials Characterization Laboratory at Sandia. We thank Jim Martin for help with magnet design and construction and George Bachand for helpful technical discussions.

6.7 References

(1) Strick, T. R.; Allemand, J. F.; Bensimon, D.; Bensimon, A.; Croquette, V. *Science* **1996**, *271*, 1835-1837.
(2) Ziemann, F.; Radler, J.; Sackmann, E. *Biophys J* **1994**, *66*, 2210-2216.
(3) Smith, S. B.; Finzi, L.; Bustamante, C. *Science* **1992**, *258*, 1122-1126.
(4) Danilowicz, C.; Coljee, V. W.; Bouzigues, C.; Lubensky, D. K.; Nelson, D. R.; Prentiss, M. *Proc Natl Acad Sci U S A* **2003**, *100*, 1694-1699.
(5) Bausch, A. R.; Ziemann, F.; Boulbitch, A. A.; Jacobson, K.; Sackmann, E. *Biophys J.* **1998**, *75*, 2038-2049.
(6) de Vries, A. H. B.; Krenn, B. E.; van Driel, R.; Kanger, J. S. *Biophys J.* **2005**, *88*, 2137-2144.
(7) Simson, D. A.; Ziemann, F.; Strigl, M.; Merkel, R. *Biophys J.* **1998**, *74*, 2080-2088.
(8) Amblard, F.; Yurke, B.; Pargellis, A.; Leibler, S. *Rev Sci Instrum.* **1996**, *67*, 818-827.
(9) Yan, J.; Skoko, D.; Marko, J. F. *Phys Rev E (Statistical, Nonlinear, and Soft Matter Physics)* **2004**, *70*, 011905.
(10) Chiou, C. H.; Lee, G. B. *J Micromech Microeng.* **2005**, *15*, 109-117.
(11) Amit, R.; Gileadi, O.; Stavans, J. *Proc Natl Acad Sci U S A.* **2004**, *101*, 11605-11610.
(12) Sniegowski, J. J.; de Boer, M. P. *Ann Rev Mater Sci.* **2000**, *30*, 299-333.
(13) Jensen, B. D.; de Boer, M. P.; Masters, N. D.; Bitsie, F.; LaVan, D. A. *J Microelectromech Syst.* **2001**, *10*, 336-346.
(14) Russick, E. M.; Adkins, C. L. J.; Dyck, C. W. *ACS Symposium Series Symposium on Supercritical Fluids - Extraction and Pollution Prevention, at the 211th National Meeting of the American-Chemical-Society; March 24-28, 1996; New Orleans, LA* **1997**, *670*, 255-269.
(15) Baselt, D.; Lee, G.; Natesan, M.; Metzger, S.; Sheehan, P.; Colton, R. *Biosens Bioelectron.* **1998**, *13*, 731-739.
(16) Reddy, S.; Moore, L. R.; Sun, L. P.; Zborowski, M.; Chalmers, J. J. *Chem Eng Sci* **1996**, *51*, 947-956.
(17) Meeker, D. C. *Finite Element Method Magnetics*, Version 3.4.2 (15Apr2005 Build), http://femm.foster-miller.net
(18) Visscher, K.; Schnitzer, M. J.; Block, S. M. *Nature* **1999**, *400*, 184-189.

Distribution

1	MS 0513	R.H. Stulen, 1000
1	MS 0887	D.B. Dimos, 1800
1	MS 1310	M.P. de Boer, 1769
1	MS 1310	A.D. Corwin, 1749
1	MS 1371	S.B. Rivera, 6928
1	MS 1371	J.M. Gaudioso, 6928
1	MS 1411	E.D. Spoerke, 1816
1	MS 1413	G.S. Heffelfinger, 8330
1	MS 1413	G.D. Bachand, 8331
1	MS 1413	P.V. Dressendorfer, 8331
1	MS 1413	B.C. Bunker, 8331
1	MS 1413	G.E. Thayer, 8331
1	MS 1413	S.J. Koch, 8331
1	MS 1413	M. Bachand, 8331
1	MS 1413	A. Carroll-Portillo, 8331
1	MS 1413	A.M. Trent, 8331
1	MS 1413	H. Liu, 8331
1	MS 1415	J.C. Barbour, 1110
1	MS 1415	N.D. Shinn, 1114
1	MS 1421	G.A. Samara, 1130
1	MS 1421	J.A. Simmons, 1130
1	MS 1427	J.M. Phillips, 1100
1	MS 9001	M.E. John, 8000
1	MS 9054	T.A. Michalske, 8300
1	MS 9404	G.D. Kubiak, 8320
1	MS 9292	M.M. Young, 8321
1	MS9292	D.Y. Sasaki, 8331
1	MS 0123	LDRD Office, 1011
1	MS 0161	Patent & Licensing Office, 11500
1	MS 9018	Central Technical Files 8945-1
2	MS0899	Technical Library, 9616